mater.scichina.com link.springer.com

Published online 12 October 2022 | https://doi.org/10.1007/s40843-022-2189-x
Sci China Mater 2022, 65(12): 3302–3323

SPECIAL ISSUE: Energy Transitions towards Carbon Neutrality

Emerging dual-atomic-site catalysts for electrocatalytic CO_2 reduction

Na Qiu[1†], Junjun Li[3†], Haiqing Wang[2*] and Zhicheng Zhang[3*]

ABSTRACT **The electrochemical CO_2 reduction reaction (CO_2RR) to yield high-value added fuels and chemicals provides a promising approach towards global carbon neutrality. Constant endeavors have been devoted to the exploration of high-efficiency catalyst with rapid reaction kinetics, low energy input, and high selectivity. In addition to the maximum metal atomic utilization and unique catalytic performance of single-atom catalyst (SAC), dual-atomic-site catalysts (DASCs) offer more sophisticated and tunable atomic structure through the modulations of another adjacent metal atom, which can bring new opportunities for CO_2RR as a deeper extension of SACs and have recently aroused surging interest. In this review, we highlight the recent advances on DASCs for enhancing CO_2RR. First, the classification, synthesis, and identification of DASCs are provided according to the geometric structure and electronic configuration of dual-atomic active sites. Then, the catalytic applications of DASCs in CO_2RR are categorized based on marriage-type, hetero-nuclear, and homo-nuclear dual-atomic sites. Particularly, the structure-activity relationship of DASCs in CO_2RR is elaborately summarized through systematically analyzing the reaction pathways and the atom structures. Finally, the opportunities and challenges are proposed for inspiring the design of future DASCs with high structural accuracy and high CO_2RR activity and selectivity.**

Keywords: dual-atomic-site catalysts, CO_2 reduction, interface engineering, electrocatalysis, heterogeneous catalysis

INTRODUCTION

The continuously excessive release of greenhouse gas, CO_2, has caused serious global climate warming and environmental degradation. In this regard, the emerging sequestration [1], chemical fixation [2], and electro/photo/thermochemical reduction technologies [3–9] have been developed to alleviate CO_2 emissions. The electrochemical CO_2 reduction reaction (CO_2RR) to yield high-value-added fuels and chemicals provides a promising approach towards an sustainable carbon-cycle utilization, especially when powered by renewable energy resources [10–17]. However, high inertness of CO_2 molecules requires a high overpotential to activate CO_2 [18–21]. The accompanying cathodic competitive hydrogen evolution reaction (HER) results in low Faradaic efficiency (FE) and selectivity in CO_2RR [22–25]. Moreover, the multiple proton-electron transformation and the C–C bond formation are usually the prerequisite for more valuable products [26–28]. To date, the efficient CO_2RR system including electrodes [27,29,30], electrolytes [31–34], and cell structures [35–37], has been pursued tirelessly. Therefore, the exploration of CO_2RR electrocatalysts with low cost and energy input as well as high FE and selectivity is urgently demanded.

Downsizing active nanoparticles to the atomic-scale site has been developed as an efficient tactic to maximize metal atomic utilization [38–41]. The emerging single-atom catalysts (SACs) have aroused significant interest in the past decade due to their exceptional catalytic performances. SACs feature inherently unsaturated coordination configuration and flexibly adjustable coordination environments [42]. The discrete energy level and highest occupied molecular orbital-lowest unoccupied molecular orbital (HOMO-LUMO) gap induced by the quantum size effect contribute to unique catalytic activity [43,44]. The appropriate support effect can not only stabilize the single atom site but also accelerate mass transport and charge transfer [45,46]. SACs have made important progress in catalyzing single-molecule elementary reactions, such as HER and oxygen evolution reaction (OER) [47,48]. The simplicity of active sites makes SACs weak in catalyzing complex multiple-molecule reactions. For instance, the high complexities in CO_2RR involving the H_2O and CO_2 co-adsorption, the multiple transformation and the C–C bond formation urgently need more sophisticated functionalities [49–51].

To largely expand the application field in catalysis, further construction of atomic-scale interfaces not only allows the advantages of SACs to be inherited, but also generates more diverse functionalized sites, thereby meeting the demands of complex reactions. Dual-atomic-site catalysts (DASCs) as a deeper extension of SACs have received great attention. Firstly, DASCs possess higher loading amounts of metal atoms, thereby leading to more favorable accessibility to active sites [49,52]. More importantly, the emerging metal-metal bond or metal-bridge atom bond possesses sophisticated tactics to modulate both electronic configuration and geometric structure of the catalysts, thus regulating the synergistic adsorption of different reactants and intermediates [53–55]. DASCs have exhibited strong multifunctionality in decoupling complex multiple-molecule reactions through providing neighboring active sites to

[1] College of Chemistry, Chemical Engineering and Material Science, Zaozhuang University, Zaozhuang 277160, China
[2] School of Chemistry and Chemical Engineering, Institute for Advanced Interdisciplinary Research (iAIR), University of Jinan, Jinan 250022, China
[3] Department of Chemistry, School of Science; Tianjin Key Laboratory of Molecular Optoelectronic Sciences, Tianjin University, Tianjin 300072, China
† These authors contributed equally to this work.
* Corresponding authors (emails: ifc_wanghq@ujn.edu.cn (Wang H); zczhang19@tju.edu.cn (Zhang Z))

break the linear scaling relationship [49,56,57]. The diversity of atomic species and valence states will provide rich combinations of two atom sites, thus providing a wider research scope for DASCs. In contrast to the numerous review articles of SACs, the systematic report on DASCs for CO_2RR, as a new research frontier, is rarely highlighted.

This review aims to highlight the recent advances on DASCs for CO_2RR applications (Fig. 1). It starts with the classification, synthesis, and identification of DASCs based on the difference in the geometric structure and electronic configuration of dual-atomic active sites. Then, the catalytic applications of DASCs in CO_2RR corresponding to marriage-type, hetero-nuclear, and homo-nuclear dual-atomic sites are categorized. Particularly, the structure-activity relationship of DASCs in CO_2RR is elaborately summarized through systematically analyzing the reaction pathways and the atom structures. Finally, the opportunities and challenges are proposed to shed light on the rational design of future DASCs with high structural accuracy and high CO_2RR activity.

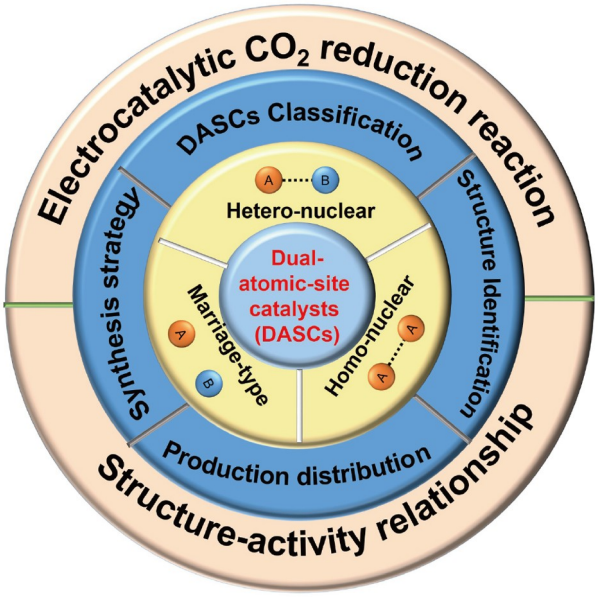

Figure 1 Overview on DASCs for electrocatalytic CO_2RR.

CLASSIFICATION, SYNTHESIS, IDENTIFICATION, AND PRODUCT DISTRIBUTION OF DASCs

Classification

Based on the spatial distribution and the metal-metal bonding, the DASCs can be classified as marriage-type, hetero-nuclear, and homo-nuclear dual-atomic sites (Fig. 2). The marriage-type DASCs feature random distribution and unrestricted spatial distances of two kinds of different isolated single-atom sites. The synergetic effects in marriage-type Fe-Co DASCs have been reported to effectively break the linear scaling relationships between *COOH and *CO to actuate CO_2RR with superior activity and high selectivity towards CO production. Different from the marriage-type DASCs, the hetero-nuclear and homo-nuclear dual-atomic sites are identified by the adjacent or neighboring two different and identical atom sites, respectively. There may or may not be metal-metal bond or bridging atom such as N between two adjacent atoms. Note that since isolated single-atom sites are usually present in DASCs, it should be suggested that only if the ratio of the paired atoms is higher than a specific ratio, such as 70%, can DASCs be well defined. Compared with marriage-type DASCs, the supplementary interactions between two adjacent sites can provide more opportunities in the regulations of geometric structure and electronic configuration to excavate great possibility of DASCs for CO_2RR.

Synthesis

The synthesis of marriage-type dual-atomic sites in DASCs shares the similar procedures with that of single-atom sites to some extent [58–60]. In contrast, the preparation of hetero-nuclear and homo-nuclear dual-atomic sites highly requires the precise control of spatial distance and coordination configuration of adjacent dual-atomic sites. Generally speaking, four strategies, i.e., mixture pyrolysis, precursor designation, thermal-control migration, and sequential deposition have been proved to effectively manipulate dual-atomic sites (Fig. 2).

The mixture pyrolysis is the simplest operation, in which only a mixture of carbon source, nitrogen source and conventional metal source is required to be calcined in inert atmosphere. The dual atoms-contained/doped metal-organic frameworks (MOFs) were extensively used as the precursors for DASC preparations [61–65]. Self-ligands and volatile Zn nodes in MOFs can provide spatial distance modulation for forming dual-atomic sites.

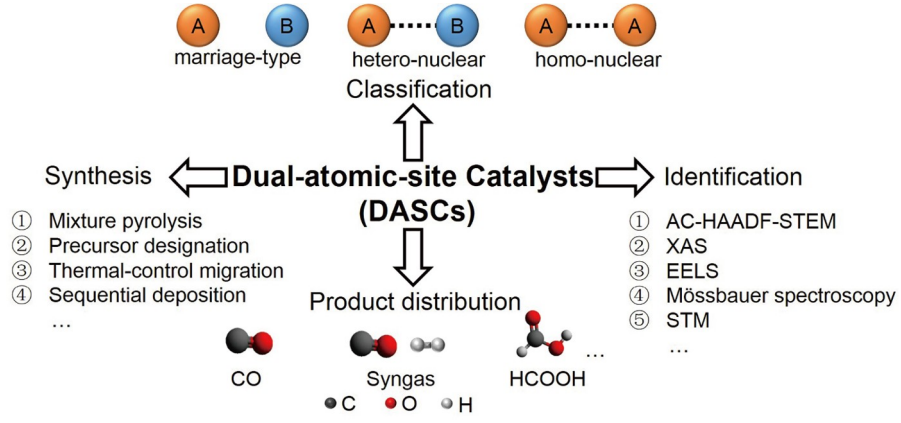

Figure 2 Classification, synthesis, identification and product distribution of DASCs for CO_2RR.

Abundant nitrogen and carbon species in MOFs can not only provide a carbonaceous support but also regulate the coordination configurations through C and/or N. Sometimes, the etching operation is necessary to remove the residual nanocrystal byproducts.

As for the precursor designation strategy, dual-atomic organic complexes have been proved to be effective precursors for the successful preparation of DASCs. The original dual-atomic structure in organic complexes is expected to be retained on the new support by the spatial segregation provided by the organic ligands. For example, the precursors of bis(1,5-cyclooctadiene) diiridium(I) dichloride ($C_{16}H_{24}Cl_2Ir_2$), dicarbonylcyclopentadienyliron ($Fe_2O_4C_{14}H_{10}$), and allylpalladium(II) chloride dimer ($(\eta_3\text{-}C_3H_5)_2Pd_2Cl_2$) have been successfully applied for the preparation of Ir_2, Fe_2, and Pd_2/mpg-C_3N_4 DASCs [50]. Dual-atom Ag_2/graphene catalyst was achieved with binuclear Ag complex {[Ag(NO_3-O)(phtz-*N*)]$_2$(μ-phtz-*N*,*N*′)$_2$} as the precursor. A more interesting aspect of the strategy is that the atom number can be well controlled from metal$_1$, metal$_2$, to metal$_3$ through utilizing inorganic compounds with corresponding atoms as precursors. For instance, mononuclear Fe/Pd, binuclear Fe_2/Pd_2, and trinuclear Fe_3/Pd_3 were achieved by using Fe(acac)$_2$/$Fe_2(CO)_9$/$Fe_3(CO)_{12}$ and $Pd(NH_3)_4(NO_3)_2$/[PdCl(C_3H_5)]$_2$/[Pd(OAc)$_2$]$_3$ as precursors, respectively [66–68].

The thermal-control migration strategy refers to the manipulation of single atom migration on the support through precisely controlled heating extent, which has been successfully practiced in the preparation of planar-like Fe_2-N_6 configuration on the carbonaceous substrate. Lower and higher heating temperatures tend to produce single-atom sites and nanoparticles, respectively. Only the appropriate temperature allows for the construction of diatomic sites.

With atomic layer deposition (ALD) apparatus, the sequential deposition of identical or different atoms can lead to the highly precise regulation of dual-atomic sites [69,70]. In order to avoid random distribution and further aggregation, the selective deposition of the second precursor is critical, which principally requires the proper selection and design of differentiated precursors and coordination sites on the substrate. Dual-atomic Pt_2 sites anchored on graphene were constructed by two-step sequential deposition, in which the steric hindrance induced by trimethyl(methylcyclopentadienyl)-platinum(IV) ($MeCpPtMe_3$) ensured the selective deposition of the second Pt in the form of immediately adjacent first-Pt atom. Therefore, the preanalysis of precursor and carrier properties, the precise control of thermal processes and the rational use of advanced equipment will help to obtain structurally controllable dual-atomic sites in DASCs.

Identification

In addition to the precise synthesis of DASCs, the identifications of geometric structure (e.g., coordination environment and spatial distance) and electronic configuration (e.g., electronic orbit and oxidation state) are very important. To date, only a limited number of advanced characterization techniques, such as aberration-corrected high-angle annular dark-field scanning transmission electron microscopy (AC HAADF-STEM), X-ray absorption spectroscopy (XAS), electron energy loss spectroscopy (EELS), and Mössbauer spectroscopy have been applied to investigate DASCs (Fig. 2) [71–73].

The imaging mechanism of AC HAADF-STEM relies on the difference in the atomic numbers between the loaded metal atoms and support atoms. Particularly, the brightness of an atom is proportional to the square of its atomic number (Z^2). AC HAADF-STEM can provide a two-dimensional (2D) projection image with an extremely high resolution down to 0.1 nm to visualize the position and distribution of dual-atomic sites. AC HAADF-STEM could work only if there is a large difference in the weights of the two atoms.

When the dual-atomic sites in DASCs have similar atomic weights or the atomic number of dual-atomic sites is less than that of substrate elements, the similar/sheltered brightness will make it difficult to distinguish the two atoms well on the AC HAADF-STEM picture. At this point, EELS has been proved to be a powerful complement to AC HAADF-STEM image, in which the signals of adjacent dual-atomic sites can be well differentiated [71].

XAS can be expanded in the usual sense to X-ray absorption near edge structure (XANES) and extended X-ray absorption fine structure (EXAFS). The collaboration of XANES and EXAFS are suggested to well reflect the average information about geometric structure and electronic configuration in DASCs. For example, the geometric structure, e.g., coordination atom/number, bridge atom, metal-metal bond and bond distance, of dual-atomic sites can be qualitatively assessed through the Fourier transform of the K space in EXAFS into R space. The electronic interactions among dual-atomic sites and support can be well achieved by analyzing XANES-derived signals about electronic orbits and valence states, in which the standard metallic and oxidized foils usually served as references.

Recently, the researchers attempted to use Mössbauer spectroscopy to parse dual-atomic sites. The doublets of D1 (low spin state), D2 (intermediate spin state), and D3 (high spin state) have been developed as the valid evidence for M-N_x sites. Particularly, Mössbauer spectroscopy has more successful practice in Fe-Co and Fe-Ni dual-atomic sites [72]. The extra peak of singlet component indicated the existence of Fe–Co bond. A new doublet (D4) can be explained by the low-spin-state Fe^{2+} or high-spin-state Fe^{3+} [73].

Taken together, each of these technologies has its own advantages and disadvantages in precisely elucidating the geometric structure and electronic configuration of dual-atomic sites in DASCs. AC HAADF-STEM can only provide a 2D and local projection image, which is greatly dependent on the large differentiation of atomic number. In contrast, both XAS and Mössbauer spectroscopy function from the perspective of bulk techniques and provide average and comprehensive information about all different types of sites in DASCs. Based on multiple characterization results, constructing theoretical models of DASCs through density functional theory (DFT) can help the reasonable optimization of dual-atomic sites by analyzing the stability of possible geometric structure and electronic configuration. Integrating the merits of different technologies may be encouraged for the analysis of DASCs. Only then can we get closer to the truth in the structure-activity relationship, thereby pursuing better development of DASCs.

Product distribution

Theoretical DFT calculation results have predicted that Cu dimers (Cu_2) anchored on porous C_2N layer can serve as promising DASCs for electrochemically converting CO_2 to hydrocarbons, such as CH_4 and C_2H_4 [55]. The Cu-based dimers supported on graphene such as Cu_2, CuMn, and CuNi, were also

theoretically evaluated for CO_2RR. Cu_2 may exhibit high activity toward CO generation. CuMn should be catalytically active toward CH_4 production. CuNi was estimated to promote the selectivity toward CH_3OH [53]. Moreover, the activity of Cu atoms with different coordination configurations and special distances for CO_2RR was also deduced. CH_4 production may tend to occur on the isolated Cu-N_4/-N_2 and neighboring Cu-N_4 sites [74]. The adjacent two Cu-N_2 sites may enable C_2H_4 generation by facilitating the coupling of two CO intermediates. Although theoretical calculations suggest that different kinds of hydrocarbon products can be synthesized through DASCs, current experimental results for CO_2RR are more likely to yield C_1 products, such as CO, syngas (a mixture of CO and H_2), and a small amount of formate. The experiments are still at an initial stage and there is still a long way to go for more advanced hydrocarbon products (Fig. 2).

DASCs FOR CO_2RR

Marriage-type DASCs for CO_2RR

Zn-La DASCs

The combination of transition metal Zn single atom and rare earth element La single atom has been achieved to prepare dual atomic Zn-La catalysts for CO_2RR. The impregnation-saturated melamine sponges with urea and metal nitrates were used as the precursors to construct Zn-La/N-doped carbon (Zn-La/NC) dual-atomic catalysts (Fig. 3a) [75]. The local coordination environments of dual atomic Zn and La were verified to be Zn–N, La–N, and La–C bonding. The ratio of CO/H_2 in syngas can be regulated from 0.14 to 1 in the potential range from −1.3 to −1.6 V by applying Zn/La single-atomic catalysts and Zn-La dual-atomic catalysts with Zn/La atomic ratios of 2:1 and 1:2 (Fig. 3b). DFT calculations have confirmed that Zn sites are mainly responsible for the activation of CO_2 towards CO product, while the H_2 evolution was promoted at La sites (Fig. 3c–e).

Ni-Fe DASCs

Another study reported that adjusting the mole ratio of Ni:(Ni+Fe) from 0, 0.2, 0.35, 0.5, 0.8 to 1.0 can well manipulate the CO/H_2 ratio of the syngas in a wide range from 0.14 to 10.86 at −0.86 V *vs.* reversible hydrogen electrode (RHE) (Fig. 3f) [76]. Based on the experimental and calculation results, the authors suggested that Fe sites in NiFe-DASCs function as a vital promoter for hydrogen production, while the protagonist for CO_2 conversion to CO should be the Ni sites.

Bi-Zn DASCs

The combination of transition-metal and main-group SACs was also reported for DASCs design. Marriage-type Bi-Zn DASCs with Bi-N_4 and Zn-N_4 configurations were also reported to be efficient for producing syngas in a wide range of CO/H_2 ratios from 0.20 to 2.92 (Fig. 3g) [77–79].

Ni-Co DASCs

Ni-Co DASCs anchored on NC were prepared through pyrolyzing the mixture of glucose, dicyandiamide, and transition metal salts [80]. The configuration of Ni-Co DASCs featured Co/Ni-pyridinic-N coordination and a negligible Co-Ni interaction. As for the single-atom Ni/Co catalyst, Ni-NC displayed an almost exclusive activity for converting CO_2 to CO (e.g., > 56 mA cm^{-2} at −1.0 V *vs.* RHE), while Co-NC exhibited a notable HER activity (e.g., >58 mA cm^{-2} at −1.0 V *vs.* RHE). Based on these observations, Ni-Co DASCs with different Co/Ni ratios were developed to regulate the CO/H_2 ratios in syngas. The performance result of CoNi-NC indicated that the CO/H_2 ratios can be adjusted in a wide range from 0.23 to 3.26, satisfying subsequent industrial thermocatalytic applications (Fig. 3h). The experimental and DFT results confirmed that Ni-NC and Co-NC are selectively responsible for CO_2 activation and H_2 evolution, respectively (Fig. 3i).

Cu-In DASCs

Considering the fact that the Cu SAC shows a low selectivity, the main-group In single-atom site was introduced into transition-metal Cu SAC to develop Cu-In DASCs [81]. As exhibited in Fig. 4a, the Cu-In DASCs were prepared through the direct pyrolysis of Cu and In multimetallic zeolitic imidazolate framework-8 (ZIF-8). The introduction of HER-inert In single-atom sites was aimed to inhibit the HER side reaction, thereby promoting the selectivity of CO_2RR to CO. The coordination configuration and valence states of Cu and In in DASCs were revealed by XANES and EXAFS. The Cu in Cu-In DASCs exhibited the average valence states in the range of 0 and +2, while the In in DASCs owned a valence state of +3. Moreover, the absent Cu–Cu, In–In, and Cu–In signals indicated the atomically dispersed Cu and In species without direct bonding between metal atoms in DASCs. The EXAFS fitting results indicate the configurations of Cu-N_4 and O_2-In-N_4 in Cu-In DASCs. The electrocatalytic CO_2RR tests of Cu-In DASCs were conducted in CO_2-saturated 0.1 mol L^{-1} $KHCO_3$ electrolyte. The FE toward CO (FE_{CO}) of Cu-In DASCs can reach up to 96% at −0.7 V *vs.* RHE (Fig. 4b), which is notably superior to the Cu or In single-atom references. The main-group In was verified to be inert for HER. Further DFT study confirmed that the Cu sites can be electronically activated by the adjacent HER-inert In sites, thus enhancing the *COOH intermediate adsorption towards CO formation pathway (Fig. 4c, d).

Hetero-nuclear DASCs for CO_2RR

Ni-Fe DASCs

Hetero-diatomic Ni-Fe site catalyst (NiFe-DASCs) composed of high-density nickel-iron atom pairs hosted on N-doped graphene was synthesized through pyrolyzing the mixture of L-alanine, melamine, and Ni/Fe acetate in argon atmosphere (Fig. 5a) [82]. XANES and EXAFS jointly verified the coexistence of Ni/Fe-N coordination and Ni–Fe bonds in the resultant NiFe-DASCs (Fig. 5b, c). The electrochemical tests revealed the roles of Fe and Ni in NiFe-DASCs for CO_2RR. Fe-SAC offered a lower onset potential but was easy to be poisoned due to the possible strong binding between CO and Fe site (Fig. 5d). Ni-SAC exhibited a higher FE_{CO} in the operated potential range (Fig. 5e). The existence of neighboring Ni atom is suggested to alleviate the poisoning phenomenon in single Fe-SAC through weakening CO adsorption strength. The further theoretical simulation indicated that the d-orbital coupling (especially $3d_{z^2}$ and $3d_{x^2-y^2}$) of hetero-diatomic nickel-iron site led to decreased orbital energy levels and delocalized electron distribution (Fig. 5f). In addition, the electron transfer from Fe to Ni and N

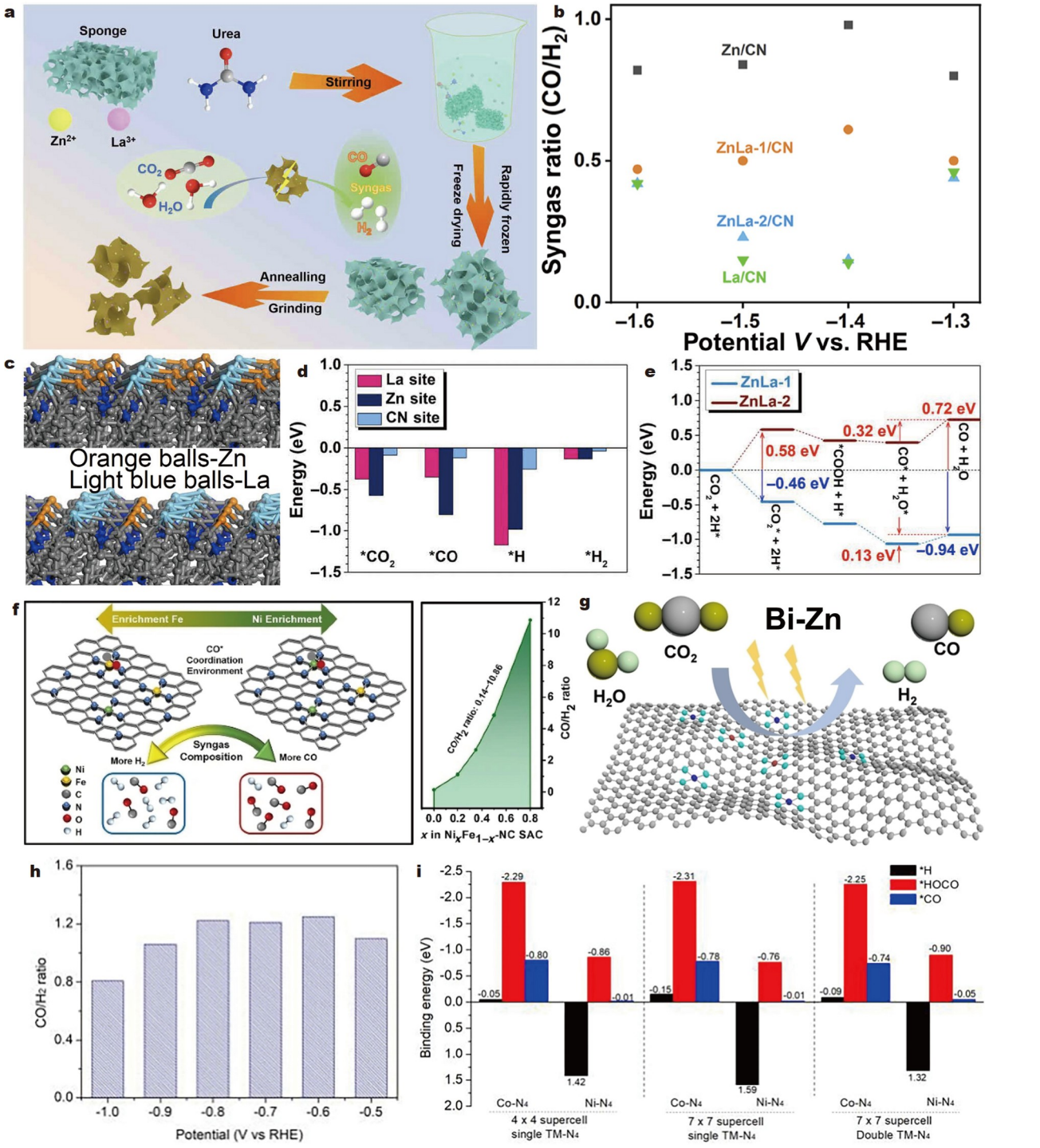

Figure 3 (a) Schematic illustration of the synthesis process of dual atomic ZnLa catalyst (Zn-La/NC). (b) The ratios of CO/H_2 for different catalysts in the potential range of −1.3 to −1.6 V *vs.* RHE. (c) The side view of relaxed structures of Zn-La/NC. (d) Adsorption energy patterns of key reactants and products of Zn-La/NC. (e) CO formation energy profile on Zn-La/NC. Reproduced with permission from Ref. [75], Copyright 2021, American Association for the Advancement of Science. (f) The relationship between the ratio of CO/H_2 in syngas and the mole ratio of Ni:(Ni+Fe). Reproduced with permission from Ref. [76], Copyright 2020, Springer. (g) Bi-Zn DASCs for electroreduction of CO_2 to syngas. Reproduced with permission from Ref. [77], Copyright 2022, Wiley. (h) Potential-dependent CO/H_2 ratios on Ni-Co DASCs. (i) Calculated binding energies on Co/Ni-N_4 centers. Reproduced with permission from Ref. [80], Copyright 2020, Wiley.

caused higher oxidation state of Fe. The above observation indicated superior characteristics for facilitating CO* desorption. As a result, NiFe-DASCs demonstrated an extraordinary activity and stability towards CO_2RR (high FE_{CO} of 94.5%, high current density of 50.4 mA cm^{-2} at an overpotential of 0.69 V, and 30 h of continuous operation) (Fig. 5e).

An isolated diatomic Ni/Fe-nitrogenated carbon (Ni/Fe-N-C) electrocatalyst was developed through the pyrolysis of MOF to

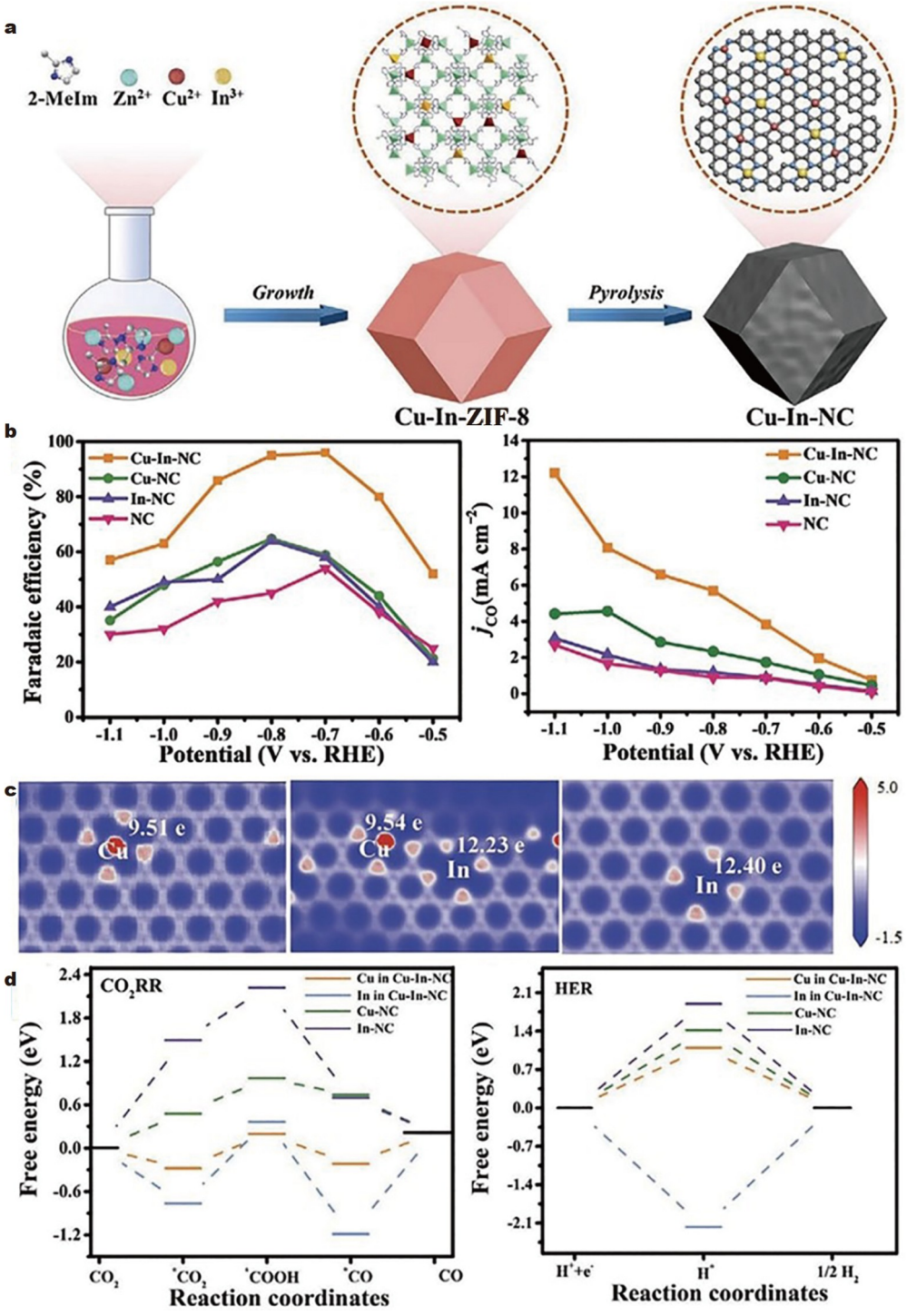

Figure 4 (a) Schematic illustration for the synthesis and the configuration of Cu and In DASCs (Cu-In-NC). (b) FE_{CO} of Cu and In DASCs at various potentials. (c) Charge density differences and (d) free energy barriers for CO_2RR and HER in Cu and In SACs, and Cu and In DASCs. Reproduced with permission from Ref. [81], Copyright 2022, Wiley.

volatilize the low-boiling-point Zn species (Fig. 5g) [83]. The collaboration of AC HAADF-STEM, XAS, and DFT calculation identify the diatomic Ni/Fe configuration and the coordination paths of Ni-N-C, Fe-N-C, and Ni-Fe in the catalyst (Fig. 5h). Compared with the deficiency of Ni-Fe path, the configuration of Fe-N_4 and Ni-N_4 is suggested to be dominant. The resultant Ni/Fe-N-C exhibited high selectivity towards CO with an FE as high as 98% at −0.7 V. The FE can be stabilized at higher than 90% throughout the tested potentials from −0.5 to −0.9 V (Fig. 5i). Moreover, Ni/Fe-N-C maintained 99% of the initial selectivity after up to 30 h testing, showing excellent catalytic stability. The designed Ni/Fe-N-C was verified to serve as an efficient electrocatalyst for converting CO_2 to CO. The electrocatalytic tests of active surface area (ECSA), Nyquist plot and Tafel plot were conducted to analyze the origin of high catalytic activity. As indicated by the lowered Tafel slop, the introduction

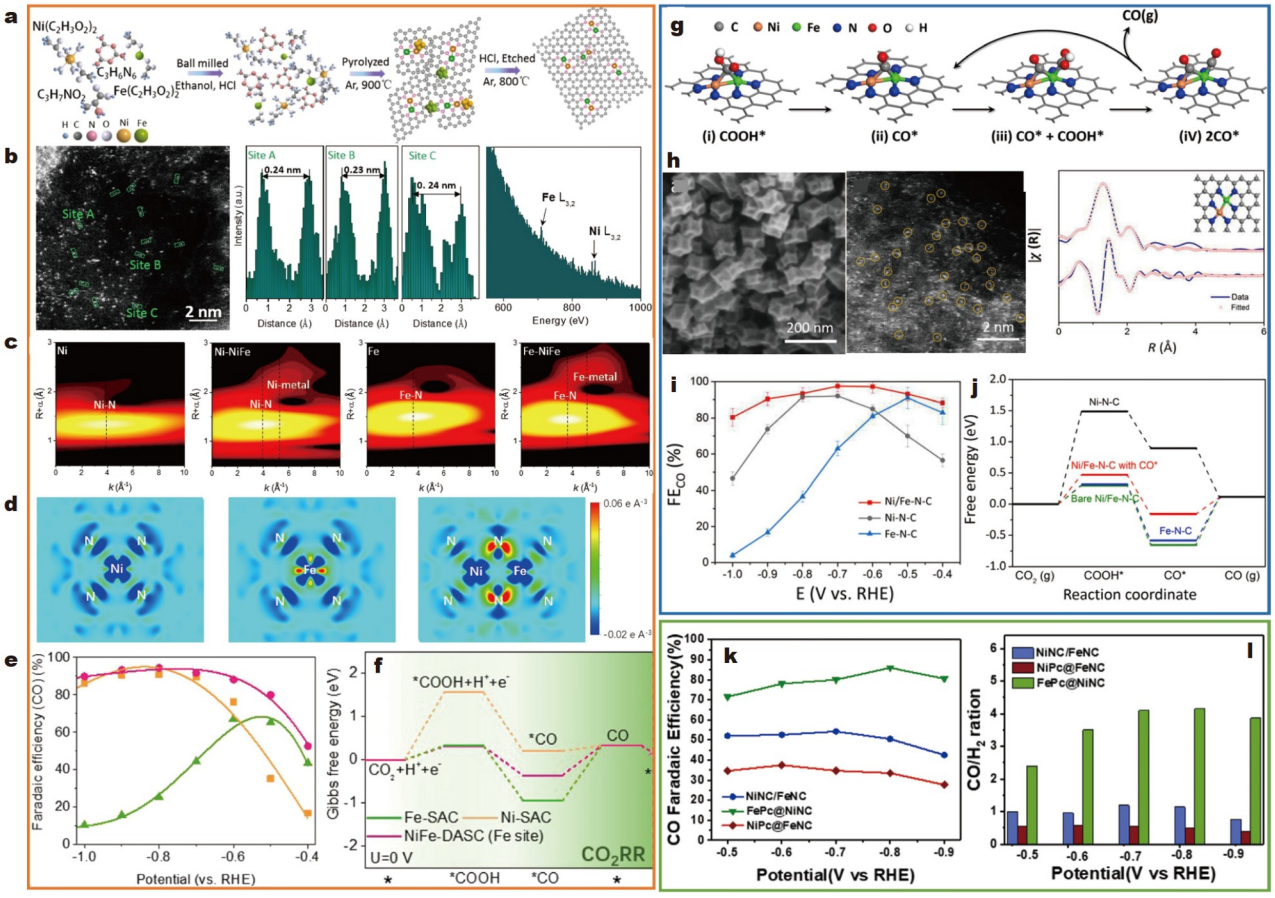

Figure 5 (a) Schematic illustration of NiFe-DASC synthesis. (b) HAADF-STEM image, the corresponding intensity profiles, and EELS analysis of NiFe-DASC. (c) Wavelet transform (WT)-EXAFS of k^2-weighted k-space spectra of Ni and Fe. (d) Differential charge density maps in NiFe-DASC. (e) FE_{CO} at various potentials. (f) Calculated free energy diagrams for CO_2RR in NiFe-DASC. Reproduced with permission from Ref. [82]. (g) Possible catalytic mechanism on NiFe-DASC. (h) Structural information of NiFe-DASC provided by SEM image, HAADF-STEM image, and Fourier transformation of EXAFS spectra. (i) FE_{CO} at various potentials. (j) The calculated free energy diagrams for CO_2RR to CO. Reproduced with permission from [83], Copyright 2019, Wiley. (k) FE_{CO} and (l) molar CO/H_2 of FePc@NiNC series catalysts at different applied potentials. Reproduced with permission from Ref. [84], Copyright 2021, Elsevier.

of Fe into Ni-N-C can significantly promote the kinetics of the first electron transfer for *COOH intermediate generation. Further DFT calculation indicated that the isolated diatomic Ni/Fe can not only provide additional active sites for the activation of the second CO_2, but also weaken the binding strength of CO* to lower the energy barrier towards CO generation (Fig. 5j).

Syngas with a suitable CO/H_2 ratio is a very important feedstock for lots of value-added chemicals. The production of syngas through the CO_2RR process is highly desirable. The manipulation of the configuration structures of bimetallic Ni-Fe SACs and the applied potentials was able to alter the molar ratios of syngas CO/H_2 production [84]. Three electrocatalysts with different types of bimetallic Ni-N and Fe-N centers were prepared. In the FePc@NiNC (NiPc@FeNC) electrocatalyst, Ni (Fe) atoms are anchored on the substrate NC matrix (NiNC/FeNC) and coordinated with iron/nickel phthalein cyanide (Fe/NiPc). The NiNC/FeNC catalyst was synthesized by simultaneously introducing Fe and Ni salts, featured with Ni and Fe anchored on the NC substrate in the form of $Ni-N_4$ and $Fe-N_4$. The resultant electrocatalytic performance indicated tunable molar ratios of CO/H_2 in syngas production from ~1:3 to ~4:1 (Fig. 5k, l). DFT calculations and experiments indicated that Fe atoms served as both the adsorption and reaction sites for CO_2 RR. However, the strong adsorption of CO* induced by single Fe sites resulted in a serious inactivation. The introduced Ni atoms are suggested to alleviate the interactions between Fe atoms and intermediate CO*, thereby optimizing the energy barriers and enhancing the stability [85].

NC hosts derived from zinc-ZIF-8 are suggested to be very flexible for the preparations of different types of Ni-Fe, Fe-Co, and Ni-Co DASCs [85]. The resultant hierarchical carbon frameworks are featured with numerous defects and N species, which are the desirable prerequisites for the adsorption and stabilization of distinctive dual metal ions (Fig. 6a). Then the formation of dual-atom sites on the NC hosts through thermal activation can be well controlled while eliminating complicated carbonization and nitrogen doping faced by traditional processes, i.e., co-pyrolyzing the mixture of carbon, nitrogen, and metal precursors. Thus, the synthesis strategy provided a full comparison among Ni-Fe, Fe-Co, and Ni-Co DASCs to deduce the possible relationship between the N-metal configuration and the CO_2RR activity and selectivity. The Ni-Fe DASC exhibited the most notable CO_2RR activity, the highest selectivity to CO and the superior stability. The coordination and configuration of

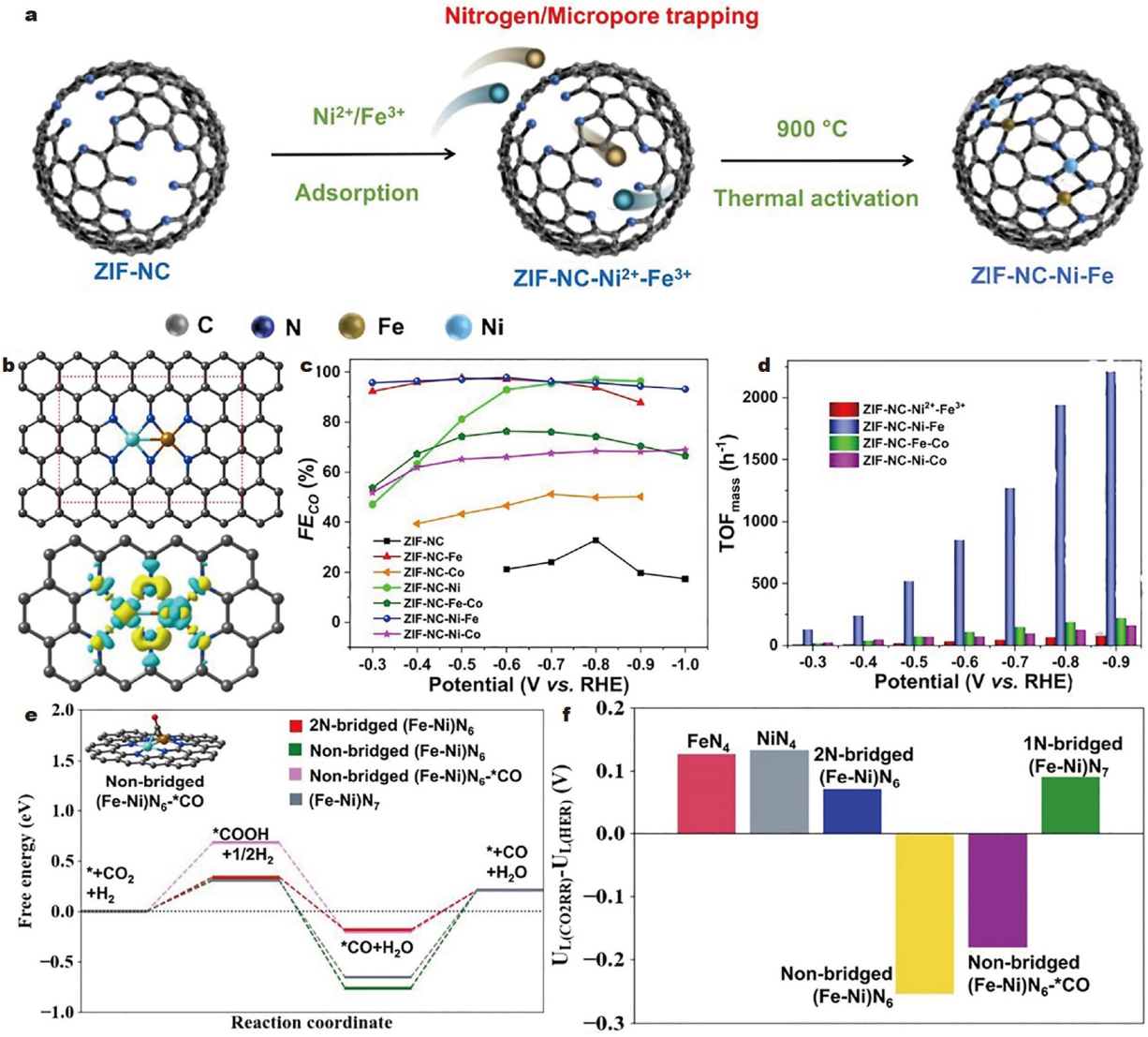

Figure 6 (a) Schematic illustration of the preparation process of NiFe-DASC in the ZIF-NC-Ni-Fe catalyst. (b) The proposed structure model and charge distribution of NiFe-DASC with two N atoms as a bridge. (c) FE_{CO} and (d) the calculated TOF values of the tested samples in 0.1 mol L^{-1} $KHCO_3$ solution. (e) Predicted CO_2RR pathways and (f) limiting potential difference between HER and CO_2RR on different catalysts. Reproduced with permission from Ref. [85], Copyright 2022, Wiley.

Ni-Fe DASC are most likely to exist in the form of 2N-bridged FeN_4 and NiN_4 moieties, i.e., (Fe-Ni)N_6 (Fig. 6b). As shown in Fig. 6c, Ni-Fe DASC displayed excellent selectivity to CO with a maximum FE_{CO} value of 97.8% at −0.6 V *vs.* RHE (Fig. 6c), which is notably higher than 76.3% of Fe-Co DASC and Ni-Co DASC. Based on the assumption that metal atoms are all active sites for CO_2RR, the turnover frequency (TOF) was calculated to evaluate the intrinsic activity of DASCs. The TOF value of Ni-Fe DASC reached up to 2210 h^{-1} at −0.9 V (Fig. 6d). The TOF values of reference Fe-Co DASC and Ni-Co DASC are about 10.0, and 13.7 times lower. DFT calculations (Fig. 6e) verified that the configuration of 2N-bridged (Fe-Ni)N_6 in Ni-Fe DASCs likely leaded to favorable *COOH adsorption and *CO desorption during the CO_2RR process through the synergy between adjacent FeN_4 and NiN_4. The calculated $U_L(CO_2RR)$-$U_L(HER)$ value of Ni-Fe DASCs is positive, implying a facilitated process for CO_2RR exceeding the competitive HER (Fig. 6f).

Ni-Co DASCs

The Co-N-Ni DASCs were developed by connecting Co and Ni atoms *via* a N bridge (Fig. 7a) [86]. Co-N-Ni DASCs own graphene-like wrinkles and ripples, in which 70% of isolated bimetallic sites were identified by AC-STEM image. The total Co-Ni content is about 0.24 wt% and the molar ratio of Co/Ni is around 1:1. Furthermore, the soft and hard XAS observations verified the local configuration of N-bridged Co-Ni dual-atom site, i.e., Co-N-Ni (Fig. 7b). Compared with TOF and FE_{CO} values of 404 h^{-1} and 45.0% in Ni single atom and 1205 h^{-1} and 61.5% in Co single atom (Fig. 7c), Co-N-Ni DASCs displayed a higher TOF of 2049 h^{-1} and FE_{CO} of 96.4% at a low potential of 0.37 V (Fig. 7d). *In situ* spectroscopy and DFT calculations implied that the generation of COOH* intermediates was accelerated by N-bridged Co-N-Ni DASCs (Fig. 7e, f), which should be responsible for the activity promotion in CO_2RR.

A pure theoretical approach of DFT and computational

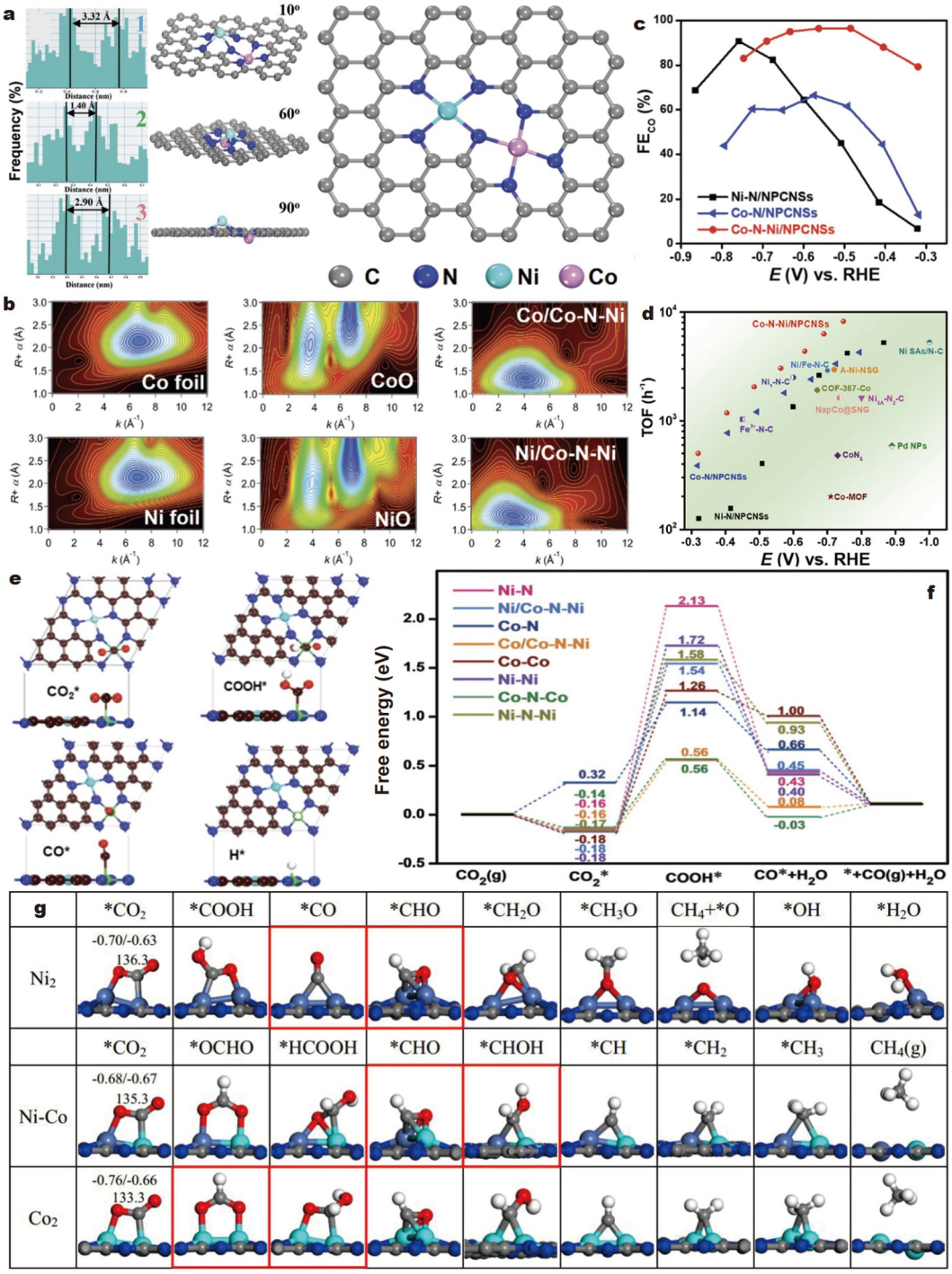

Figure 7 (a) Schematic models of different Co-N-Ni diatomic distances at different angles. (b) WT plots at the Co and Ni K-edges. (c) FE_{CO} at different applied potentials. (d) TOF comparison of different samples. (e) Structure and adsorption configurations of key intermediates on Co-N-Ni. (f) Free energy diagrams for CO_2RR to CO. Reproduced with permission from Ref. [86], Copyright 2021, the Royal Society of Chemistry. (g) DFT-optimized structures of $Ni_2@C_2N$, $Co_2@C_2N$ and $NiCo@C_2N$ along the primary reaction pathway of CO_2RR towards CH_4 formation. Reproduced with permission from Ref. [87], Copyright 2019, American Chemical Society.

hydrogen electrode was developed to explore the synergy of heterometallic $NiCo@C_2N$ graphene matrix, homometallic $Ni_2@C_2N$ graphene matrix and $Co_2@C_2N$ graphene matrix for catalyzing CO_2RR (Fig. 7g) [87]. The heterometallic $NiCo@C_2N$ was suggested to be most active in converting CO_2 molecules towards CH_4 by evaluating the limiting potentials. The intimate metal-metal bonding and the 3d-state electronic resonance in Ni-Co dimer sites were demonstrated to elicit the synergy effects in $NiCo@C_2N$.

Cu-Fe DASCs

Copper(II) phthalocyanine (CuPc)-modified Fe-ZIF-8 (PcCu-

Fe-ZIF-8) was used as the precursor to prepare a dual-atomic-site Cu-Fe electrocatalyst through the pyrolysis procedure under Ar atmosphere (Fig. 8a) [88]. The activities of the intended Cu-Fe-N_6-C and the reference Cu-N-C and Fe-N-C were tested for CO_2RR in CO_2-saturated 0.1 mol L^{-1} $KHCO_3$ (Fig. 8b). Cu-Fe-N_6-C displayed an FE_{CO} value of 98% at −0.7 V, which is higher than 65% of Fe-N-C at −0.9 V and 21.7% of Cu-N-C at −0.6 V. The electrochemical impedance spectroscopy (EIS) and Tafel plots indicated a faster CO_2RR kinetics for Cu-Fe-N_6-C. The X-ray photoelectron spectroscopy (XPS) and EXAFS results indicated that the coordination states in Cu-Fe DASCs should exist in three types of Fe-N, Cu-N, and Cu-Fe (Fig. 8c). However, it is hard to discriminate the relative spatial location of Cu and Fe by EXAFS. Based on the spectroscopic results, the structural model of CuN_3-FeN_3 (Cu-Fe-N_6-C) was built to unveil the potential structure-activity relationship in Cu-Fe DASCs for CO_2RR. DFT calculations further verified that the Fe site breaks C–O in COOH* to form CO*, while the OH* transfers to the adjacent Cu site (Fig. 8d). The bifunctional roles of Cu-Fe-N_6-C in promoting CO_2RR activity were proposed through facilitating the adsorption of CO_2 and decreasing the breaking barrier of C–O bonds.

The pyrolysis of Cu- and Fe-doped ZIF-8 was also developed for preparing CuFe-N_6 (Cu-Fe DASCs) anchored on nitrogen-carbon substrate catalysts (Fig. 8e). The CuFe-N_6 diatomic catalysts showed maximum FE_{CO} of 95.5% at −0.40 V *vs.* RHE and a relatively high energy efficiency of about 78.3% (Fig. 8f) [89]. The EXAFS result indicated the presence of Cu–N, Fe–N and Cu–Fe bonds with coordination numbers of ~3, ~3 and ~1, respectively. The conversion step from CO_2 to *COOH was suggested to be the rate-limiting step for CO_2RR in the case of CuFe-N_6. The simulation indicated that CuFe-N_6 can present enhanced adsorption for *COOH intermediates. Simultaneously, the coordinated Cu with Fe is favorable to mediate the C–Fe bond, leading to a moderate adsorption energy for *COOH. In addition, the extra pyridine N sites are also active for the CO_2RR pathway. The above cooperative effects in CuFe-N_6 demonstrate the fast kinetics and the optimal intermediate

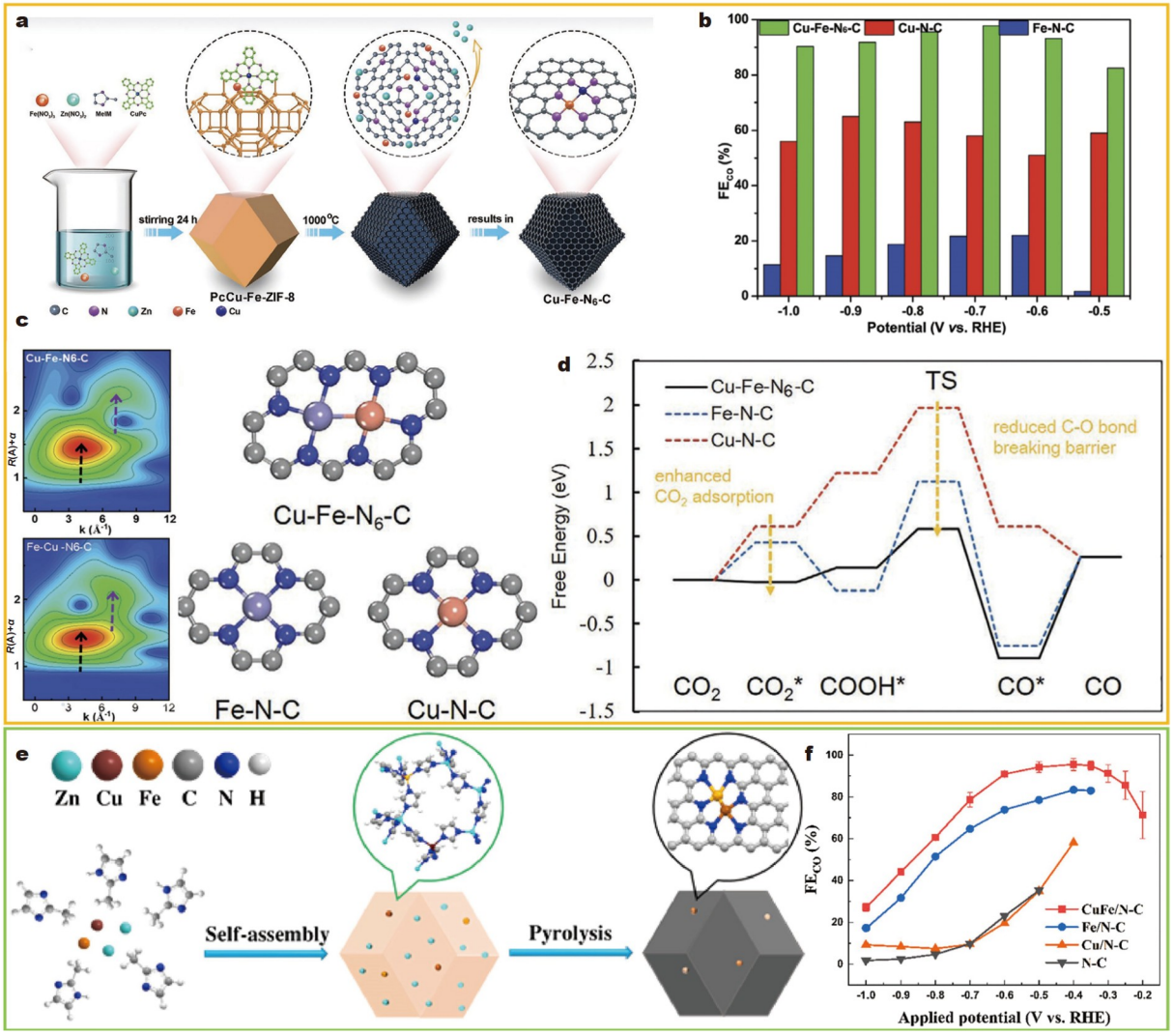

Figure 8 (a) Schematic illustration for the preparation of Cu-Fe-N_6-C. (b) FE_{CO} of Cu-Fe-N_6-C at different potentials. (c) WT plots of Cu-Fe-N_6-C and the corresponding models. (d) Free energy profiles for CO_2RR on Cu-Fe-N_6-C. Reproduced with permission from Ref. [88], Copyright 2021, Wiley. (e) Schematic illustration for the preparation of CuFe/N-C (CuFe-N_6). (f) FE_{CO} of CuFe/N-C at various applied potentials. Reproduced with permission from Ref. [89], Copyright 2020, Elsevier.

adsorption for CO_2RR.

Another MOF-derived hetero-nuclear Fe-Cu DASC showed a superior FE_{CO} of >95% from −0.4 to −1.1 V *vs.* RHE and reached the maximum 99.2% at −0.8 V *vs.* RHE [63]. The TOF value was estimated to be 5047 h^{-1} at −1.1 V *vs.* RHE. Further DFT calculations suggested that the position of d-band center in metal sites can be effectively modulated through the interactions between the adjacent Fe and Cu diatoms, thus optimizing the *COOH formation energy and *CO desorption energy in the CO_2RR reaction route towards CO.

Ni-Cu DASCs

Ni-Cu DASCs were prepared based on Ni-Cu bimetallic MOFs, in which Ni and Cu served as the metal nodes. When compared with the strategies of mixing metal anchoring and two-step doping, the relative spatial position and distance between bimetallic Cu and Ni active centers can be well classified and adjusted (Fig. 9a) [90]. The Ni-Cu DASCs demonstrated well-arranged neighboring Cu and Ni sites with Cu-N_4 and Ni-N_4 coordination conditions (Fig. 9b). When the catalysts were tested in CO_2RR, the FE_{CO} of Ni-Cu DASCs reached up to 99.2% at −0.79 V *vs.* RHE and was stably higher than 95% in the range of measuring overpotentials from −0.39 to −1.09 V *vs.* RHE, achieving remarkable catalytic activity and selectivity (Fig. 9c). The DFT calculations and Tafel results showed that the generation of *COOH was the rate-limiting step for converting CO_2 to CO in this catalysis system (Fig. 9d). In detail, the adsorption of *COOH was suggested to be preferential on the Ni sites of Ni-Cu DASCs. The neighboring Cu-N_4 sites can lead to a synergistic effect towards Ni by lowering the energy barrier for CO_2 activation. Thus, the formation rate of rate-limiting *COOH intermediates was accelerated in Cu-N_4/Ni-N_4 diatomic catalysts.

The same coordination configuration of Cu-N_4 and Ni-N_4 in Ni-Cu DASCs was also constructed by the sequential electrospinning and chemical vapor deposition technologies [91]. The Ni-Cu DASCs displayed a notable FE_{CO} of 99.6% at an operated potential of −0.98 V *vs.* RHE. The activity promotion in this case was discussed from the perspective of electronegativity offset between the neighboring Ni and Cu atoms. Specifically, the electronegativity compensation can trigger strong electron interactions in Ni-Cu DASCs, which can accelerate the formation of the *COOH intermediate, thereby decreasing the reaction energy barrier for CO_2RR.

A novel Ni-Cu DASCs with quasi-covalently coupled Ni-N_3 and Cu-N_3 configurations was prepared through the pyrolysis of Cu/1,10-phenanthroline complex-doped Ni-ZIF-8. The theoretical screening indicated that the introduction of secondary Cu atom into the Ni SAC can lead to a promoted *COOH formation, i.e., the rate-determining step for CO_2RR in this case, by ascending the orbital energy of the Ni 3d to the Fermi level. In addition, the presence of Cu can inhibit the competing HER due to its intrinsic inactivity towards water dissociation. Thus, the synergistic effect in Ni-Cu DASCs with Ni-N_3 and Cu-N_3 configuration displayed a record-high TOF value of 20,695 h^{-1} and FE_{CO} of 97.7% at −0.6 V *vs.* RHE [92].

Ni-Sn DASCs

Sn-based CO_2RR electrocatalysts have been previously reported for formate production. Ni-Sn DASCs was reported as one of the few catalysts that can produce formate [62]. The Ni-Sn dual atomic sites were prepared *via* continuous pyrolysis treatment of Zn-MOF arrays and the mixture of metal source and NC nanosheets (Fig. 9e). The HAADF-STEM and XAS characterizations verified the atomically accurate N_4-Ni-Sn-N_4 configuration in Ni-Sn DASCs (Fig. 9f). Ni-Sn DASCs displayed an $FE_{formate}$ of 86.1%, which is notably higher than 70.4% of Sn-SAC and <1% of Ni-SAC at −0.82 V *vs.* RHE with 0.5 mol L^{-1} $KHCO_3$ as the electrolyte (Fig. 9g). An *in situ* electrochemical method was used to quantitatively characterize the active site density. The availability of active sites in Ni-Sn DASCs reached up to 57.9%, which was almost twice as large as the powder sample (32.7%). DFT calculations concluded that the intrinsic active site for converting CO_2 to formate in Ni-Sn DASCs was the Sn site, and the neighboring Ni site enabled positively charged Sn site in Ni-Sn DASCs (Fig. 9h). Interestingly, the synergy of Ni and Sn can not only facilitate the CO_2 adsorption but also impose a spontaneous thermodynamic transformation of *OCHO. Thus, Ni-Sn DASCs demonstrated a synergistic advantage in handling complex multiple-intermediates and multiple-electron-involved reactions, which will shed light on the design of CO_2RR electrocatalysts towards a richer range of products.

Zn-Co DASCs

The neighboring Zn and Co monomers coordinated on NC (ZnCoNC) were prepared through the pyrolysis of mixed zinc source, cobalt source, carbamide and carbon black [93]. The collaboration of inductively coupled plasma optical emission spectroscopy (ICP-OES), XPS and energy dispersive spectroscopy (EDS) mapping indicated a composition of Zn-0.35 wt%, Co-0.72 wt%, N-3.12 wt% and C-95.42 wt% in ZnCoNC. The coordination environment and the electron effects of Zn and Co monomers were explored by XANES and EXAFS. The peak position and the fitting plot confirmed that the Zn and Co were both coordinated on NC (Zn-N and Co-N) in a tetra-coordinated form (Zn-N_4 and Co-N_4). The direct metal-metal bonding between Zn and Co and the metal-C coordination were excluded. Most of Co and Zn atoms in ZnCoNC interact indirectly through N atoms. Thus, the resultant ZnCoNC can serve as an ideal model to investigate the electronic effect of two neighboring isolated atoms for electrocatalytic CO_2 reduction. Notably, compared with the reference single-atom Co (CoNC) and Zn (ZnNC) samples, ZnCoNC displayed lower onset potentials and higher current densities. The FE of ZnCoNC reached up to 93.2% at −0.5 V in CO_2-saturated 0.5 mol L^{-1} $KHCO_3$ solution, markedly outperforming 56.3% of ZnNC and 67.3% of CoNC (Fig. 9i). A 30-h test of long-time stability indicated no decay of FE (over 90%) and CO partial current density (about 26 mA cm^{-2}). Based on attenuated total reflectance-infrared spectrometer (ATR-IR) measurements and DFT calculations, the authors analyzed the overall reaction rate by considering the key processes of *COOH adsorption and *CO desorption on the Zn and Co monomers (Fig. 9j). The single-atom sites in CoNC and ZnNC do not handle with the adsorption and desorption of the two different intermediates very well. The close isolated diatomic Zn and Co in ZnCoNC were suggested to balance the reaction pathway by mediating the transfer and conversion of *COOH and *CO. The *COOH should firstly adsorb on the Co site and convert to *CO, and then the *CO transfers to the Zn site and dissociates from Zn, thus offering an optimized activity in electrocatalytic CO_2 reduction.

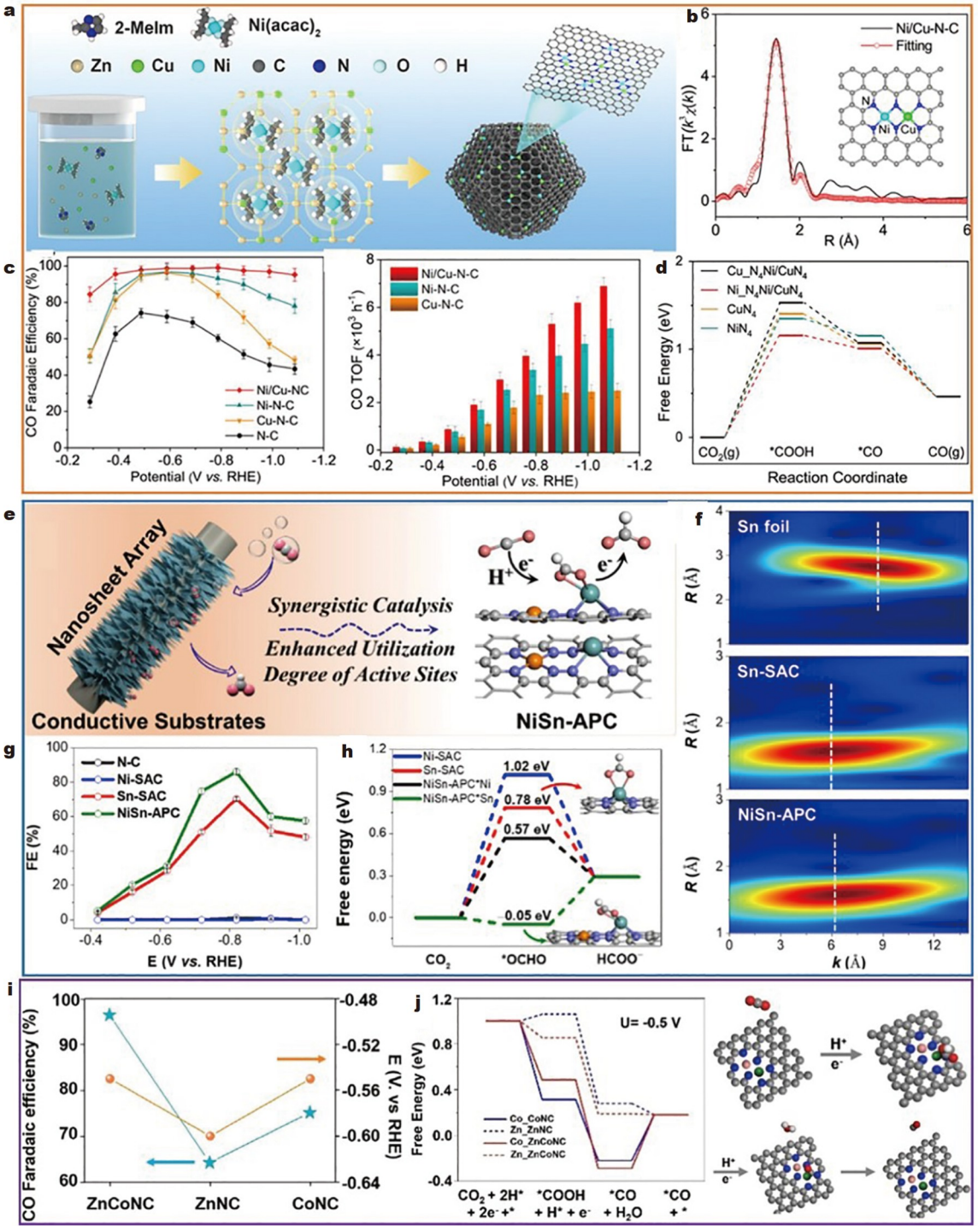

Figure 9 (a) Schematic illustration of Ni/Cu-N-C (Ni-Cu DASCs) fabrication. (b) K-edge EXAFS fitting curve of Ni/Cu-N-C in the R space. (c) FE_{CO} and calculated TOF for catalysts at different potentials. (d) Free energy profiles of the CO_2RR. Reproduced with permission from Ref. [90], Copyright 2021, American Chemical Society. (e) Scheme illustration for Ni-Sn DASCs. (f) EXAFS WT image of Ni-Sn DASCs. (g) $FE_{formate}$ at various applied potentials. (h) Free energy diagrams in CO_2RR for formate production. Reproduced with permission from Ref. [62], Copyright 2020, Wiley. (i) Maximum FE at corresponding potentials of Ni-Sn DASCs. (j) Calculated free energy for CO_2RR pathway. Reproduced with permission from Ref. [92], Copyright 2020, Wiley.

Fe-Co DASCs

The cases above are all based on in-plane DASCs catalysts. Here we would like to categorize separately a case in order to inspire the design of non-planar DASCs catalysts. The non-planar CoPc©Fe-N-C was prepared through a sequential pyrolysis and post-impregnation strategy (Fig. 10a) [94]. Firstly, Fe-N sites were prepared through the pyrolysis of Fe-ZIF-8. After that, cobalt phthalocyanine (CoPc) was impregnated into the Fe-N-C. Compared with CoPc and CoPc©Zn-N-C reference samples, the characterizations indicated the promoted oxidation state and the decreased symmetry in CoPc of CoPc©Fe-N-C. The observation strongly indicated a notable interaction between the CoPc

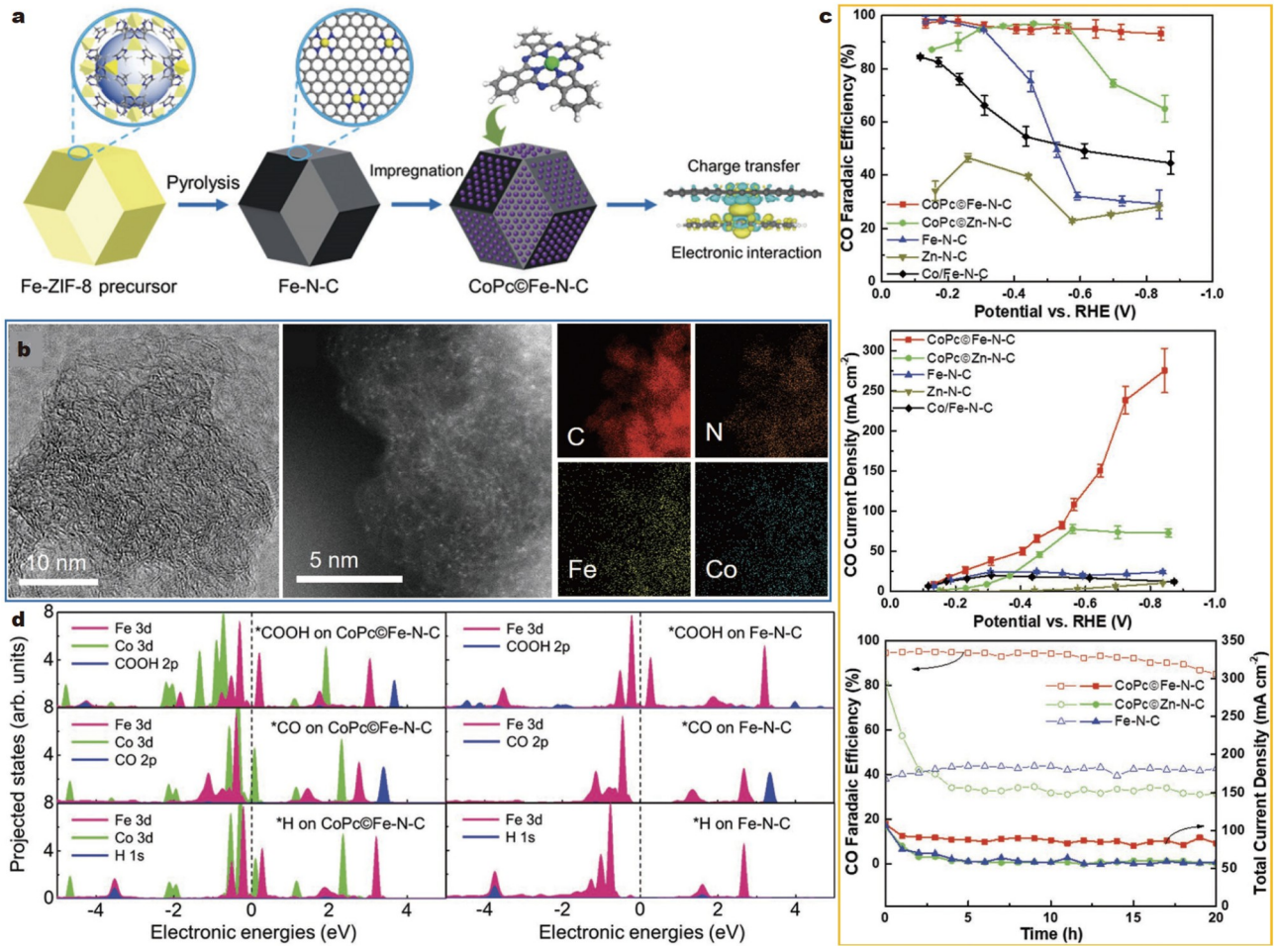

Figure 10 (a) Schematic illustration for the preparation of CoPc@Fe-N-C. (b) HRTEM, high-resolution HAADF-STEM, and EDS mapping images of CoPc@Fe-N-C. (c) FE_{CO}, CO partial current density, and stability test over different catalysts. (d) Projected density of states (PDOS) of *COOH, *CO, and *H adsorption on different sites. Reproduced with permission from Ref. [94], Copyright 2019, Wiley.

molecule and Fe-N-C substrate in CoPc©Fe-N-C (Fig. 10b). The synergy between non-planar single atom Co and Fe in CoPc©Fe-N-C displayed a high FE_{CO} over 90% in a wide potential range from −0.13 to −0.84 V *vs.* RHE, and approximately 10- and 2.5-times promotion in CO current density was observed when compared with Fe-N-C and CoPc©Zn-N-C, respectively (Fig. 10c). DFT calculation results implied that the adjacent CoPc can not only promote the CO desorption, but also suppress the competing HER at Fe-N sites (Fig. 10d). Therefore, the non-planar CoPc©Fe-N-C DASCs catalysts offered an inspiring collaboration toward CO_2RR.

Homo-nuclear DASCs for CO_2RR

Cu_2 DASCs

A stable Cu_2 atom-pair anchored on the surface of $Pd_{10}Te_3$ alloy nanowires by Te defects was developed for CO_2RR (Fig. 11a) [95]. It should be noted that this is one of the few cases where a diatomic catalyst has been constructed without using NC as the substrate. The actual loading ratio of Cu was determined to be 0.10 wt%. XAFS spectroscopy and theoretical calculation results verified that the Cu species are atomically dispersed with the bonding of Cu–O, Cu–Cu and Cu–Pd. Moreover, the partially oxidized Cu^{x+} also exists. The most probable conformation of Cu was suggested to be Cu_4-O_x, where the two Cu atoms at the bottom are responsible for stabilizing Cu_4, and the surface Cu_2 acts as the active sites to directly participate in CO_2RR. Specially, one atom in Cu_2 exists in the form of Cu^{x+} by binding with O, which further coordinates with an adjacent Cu to establish Cu_1^0-Cu_1^{x+} atom pair catalyst (Cu-APC) (Fig. 11b). The dynamics of the atomic structure in Cu-APC was investigated at the solid-liquid interface during the electrocatalysis. The results confirmed that Cu_1^{x+} in Cu-APC adsorbs water molecules, which leads to the synergistic adsorption of CO_2 molecules by the neighboring Cu_1^0, thus achieving efficient activation of CO_2 molecules. As for the catalytic activity in CO_2RR, the undoped $Pd_{10}Te_3$ nanowires present a low FE_{CO} of below 17% but strong hydrogen evolution under all applied potentials. The FE_{CO} of doped Cu-APC nanowires with optimal Cu-0.10% loading reached up to 92% at −0.78 V in 0.2 mol L^{-1} $NaHCO_3$ solution (pH 7), and the HER was greatly suppressed judging from merely 3% of FE_{H2} (Fig. 11c). The 3-h stability assessment of Cu-APC at −0.78 V displayed virtually unchanged current density and a satisfactory FE_{CO} of 80%, indicative of robust Cu-APC in CO_2RR. As indicated by the results of experiments and DFT calculations (Fig. 11d), Cu_1^0-Cu_1^{x+} in Cu-APC can simultaneously promote both the kinetics and thermochemistry for CO_2 activation through lowering the free energy barrier (ΔG) and

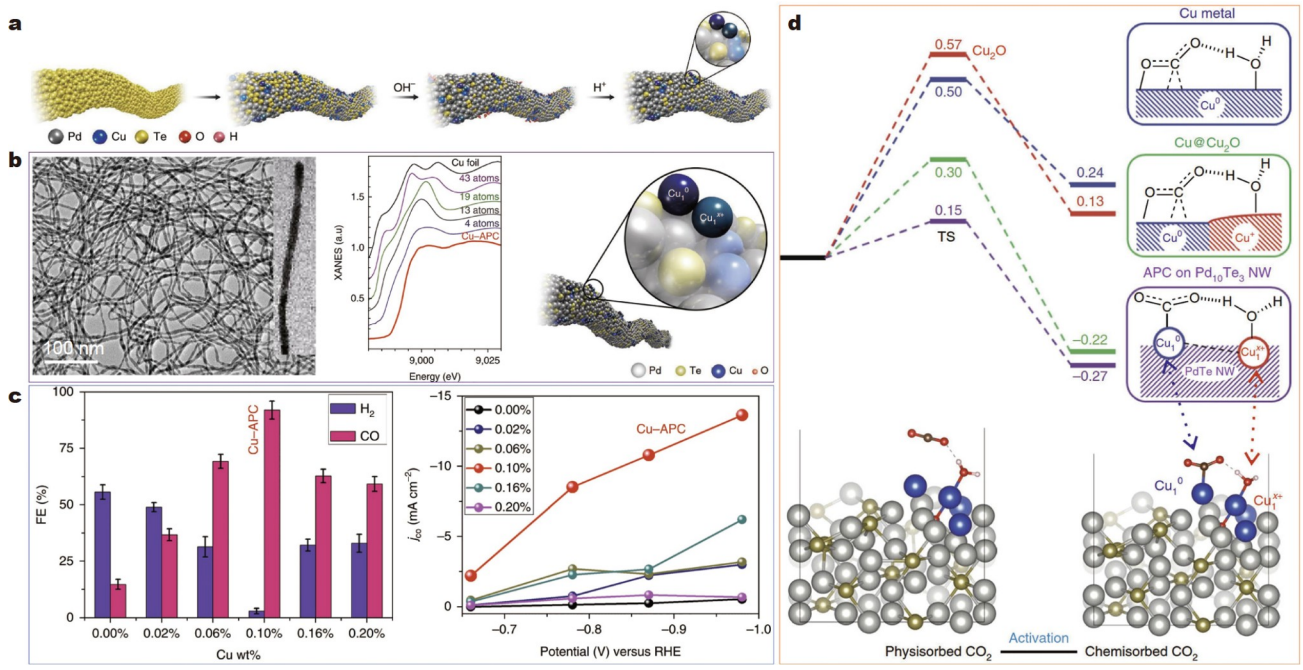

Figure 11 (a) Schematic illustration of the fabrication procedures of Cu-APC. (b) TEM image (left), the corresponding XANES spectra of Cu-based samples with varying numbers of Cu atoms (middle), and the proposed structure (right) of Cu-APC. (c) FE_{CO} and FE_{H_2} of different Cu-loaded samples at −0.78 V *vs.* RHE (left) and CO current densities under different potentials (right). (d) Free energy profiles for CO_2 activation mode. Reproduced with permission from Ref. [95], Copyright 2019, Nature Publishing Group.

stabilizing the negative charge on chemisorbed CO_2, respectively.

Fe_2 DASCs

As for non-noble Fe single atoms, typically with a Fe-N-C configuration, they demonstrated low overpotentials for CO_2 conversion to CO [96]. However, the strong adsorption of *CO intermediate on Fe-N-C sites hindered the CO desorption, thus resulting in sluggish reaction kinetics. In order to break the linear scaling relationships in the case of Fe-SAC, dual-atom Fe_2 anchored on NC matrix was developed by pyrolyzing Fe-ZIF-8 (Fig. 12a) [97]. The configuration of Fe_2-N_6-C was confirmed by XAFS measurements (Fig. 12b). In addition, The DFT calculations and the CO_2 and CO temperature-programmed desorption (TPD) experiments certified the difference in CO_2 and *CO adsorption between Fe-N-C and Fe_2-N_6-C structures (Fig. 12c). Especially, compared with the strong adsorption of *CO on single-atom Fe, the orbital coupling between the dual-atom Fe_2-N_6-C reduces the energy gap between the antibonding and bonding states of Fe–C bond, thereby facilitating the desorption of *CO. The Fe_2-N_6-C achieved higher FE_{CO} of over 80% in a wide range of tested potentials from −0.5 to −0.9 V *vs.* RHE, compared with single-atom Fe-N-C counterparts (Fig. 12d). The TOF value of Fe_2-N_6-C was up to 26,637 h^{-1} (at −1.0 V), which was 2.84 times that of Fe-N-C. Moreover, compared with the notable decay in both FE_{CO} and current density in Fe-N-C, Fe_2-N_6-C retained about 95.85% of the initial FE_{CO} and displayed imperceptible change in the total current density during 21 h of continuous operation.

Pd_2 DASCs

Pd-based CO_2RR electrocatalysts have demonstrated high catalytic activity and high selectivity towards CO. However, the easily formed PdH species make HER highly competitive at the operated electrochemical potentials. The FE_{CO} for Pd-based SACs is generally less than 60%, which is far from satisfactory. Recently, Wang's group [98] reported a Pd_2 DASCs for the first time towards CO_2RR (Fig. 13a). The Pd_2 dual-atom sites were anchored on acetylene black through an anion replacement deposition-precipitation strategy. The AC HAADF-STEM image confirmed the isolated Pd dual atoms and the EXAFS spectrum verified the unchanged coordination environment of Pd_1 SAC and Pd_2 DASCs during the preparation procedure (Fig. 13b). The maximum values of FE_{CO} for the reference Pd nanoparticle (Pd_{NP}) and Pd_1 SAC samples were below 80% and 65%, respectively, in the potentials from −0.7 to −0.95 V. By contrast, the Pd_2 DASCs exhibited a consistent high FE_{CO} of >80%, and a maximum FE_{CO} value of 98.2% was achieved at −0.85 V *vs.* RHE (Fig. 13c). The Tafel slop results proved that the activation of CO_2 molecules was the rate-limiting step. The DFT calculations of Pd_1, Pd_2, and Pd_{NP} models indicated that the Pd_{NP} presented strong CO* adsorption while the Pd_1 owned weak CO* adsorption (Fig. 13d, e). The moderate adsorption strength of CO* was observed on the Pd_2 DASCs sample, almost located at the top of the volcano plot. In addition, Bader charge analysis indicated that Pd_2 DASCs had the lowest oxidation state and transferred more electrons to CO* due to the presence of electron transfer between Pd_2 atoms (Fig. 13f).

Ni_2 DASCs

The Ni_2 DASCs were synthesized by a dinuclear-cluster-derived strategy, which can be summarized in two steps. Firstly, ligand-protected $Ni_2(dppm)_2Cl_3$ (dppm = bis(diphenylphosphino) methane, $Ph_2PCH_2PPh_2$) diatomic cluster was prepared as the metal precursor (Fig. 14a) [64]. Ni_2 DASCs were then achieved after the pyrolysis carbonization of $Ni_2(dppm)_2Cl_3$ impregnated

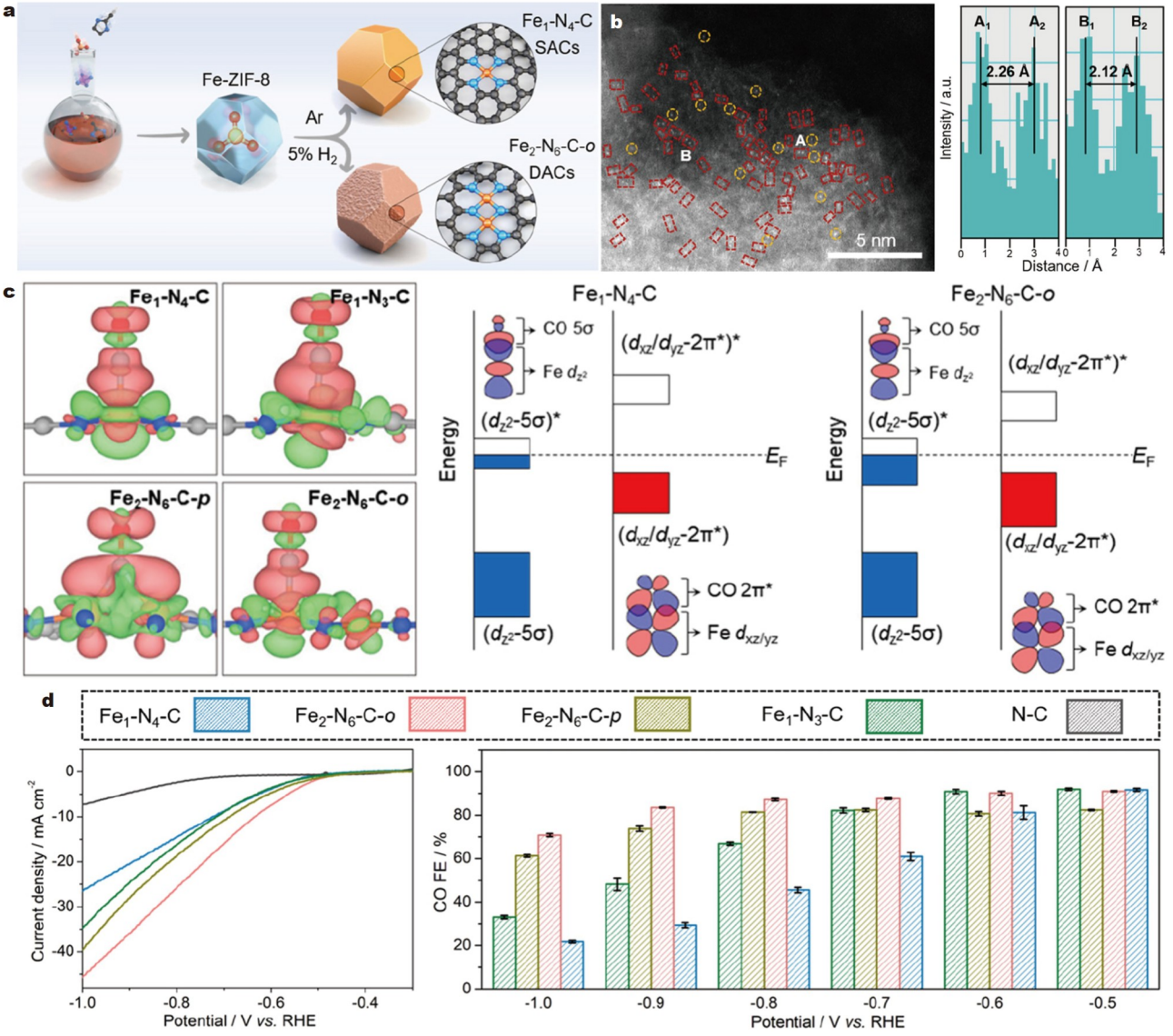

Figure 12 (a) Schematic of the preparation process of Fe_2-N_6-C (denoted as Fe_2-N_6-C-*o* in the original paper). (b) AC HAADF-STEM image and the corresponding intensity profiles obtained on the two sites in areas A and B. (c) *CO adsorption on Fe_1-N_4-C and Fe_2-N_6-C. (d) The LSV curves (left) and FE_{CO} (right). Reproduced with permission from Ref. [97], Copyright 2022, American Chemical Society.

ZIF-8-derived porous NC substrate. The Ni content for Ni_2 DASCs (Ni_2/NC) was measured to be approximately 0.18 wt% according to the ICP-OES analysis. HAADF-STEM image indicated the existence of dinuclear Ni_2 site, and the spatial distance between the neighboring Ni atoms was about 2.9 Å, which well retained the pristine 2.63 Å distance in $Ni_2(dppm)_2Cl_3$. The configuration of Ni_2 in Ni_2 DASCs was suggested to be Ni_2-N_6, in which two N atoms bridged the adjacent two Ni_1-N_4 configurations (Fig. 14a). As for the activity of Ni_2 DASCs in CO_2RR, 94.3% FE_{CO} was obtained at the current density of 150 mA cm^{-2} in the CO_2-flowed 1.0 mol L^{-1} $KHCO_3$ electrolytes, which was about 1.3 and 10.6 times higher than those of Ni_1/NC and NC reference samples, respectively (Fig. 14b). After 50 h of continuous electrolytic operation, approximately 91% FE_{CO} was still maintained, implying the reasonable structural stability of Ni_2 DASCs. *Operando* XAFS characterization indicated that the applied voltage can trigger the transformation of Ni_2 configuration from static Ni_2-N_6 to O-Ni_2-N_6 *via* oxygen-bridge adsorption. As the applied voltage became more negative, the distance between two adjacent Ni atoms will be further compressed by the oxygen-bridge adsorption, leading to an optimized structure and enhanced Ni–Ni interaction. The O-Ni_2-N_6 configurations were suggested to significantly promote the performance of Ni_2 DASCs in CO_2RR towards CO by lowering the energy barrier for the activation of CO_2 reactant to COOH* intermediate (Fig. 14c). It is noteworthy that in this study the authors applied a comprehensive collection of *operando* XAFS, *operando* Fourier transformed infrared spectroscopy (FTIR), XANES simulation, and DFT calculation for the first time to elucidate the changes in dinuclear active site and intermediate conformation throughout the reaction process.

The Ni_2 DASCs with different Ni_2 configurations were prepared by a two-step electrostatic spinning-pyrolysis method (Fig. 14d) [99]. The HAADF-STEM and XAFS characterizations

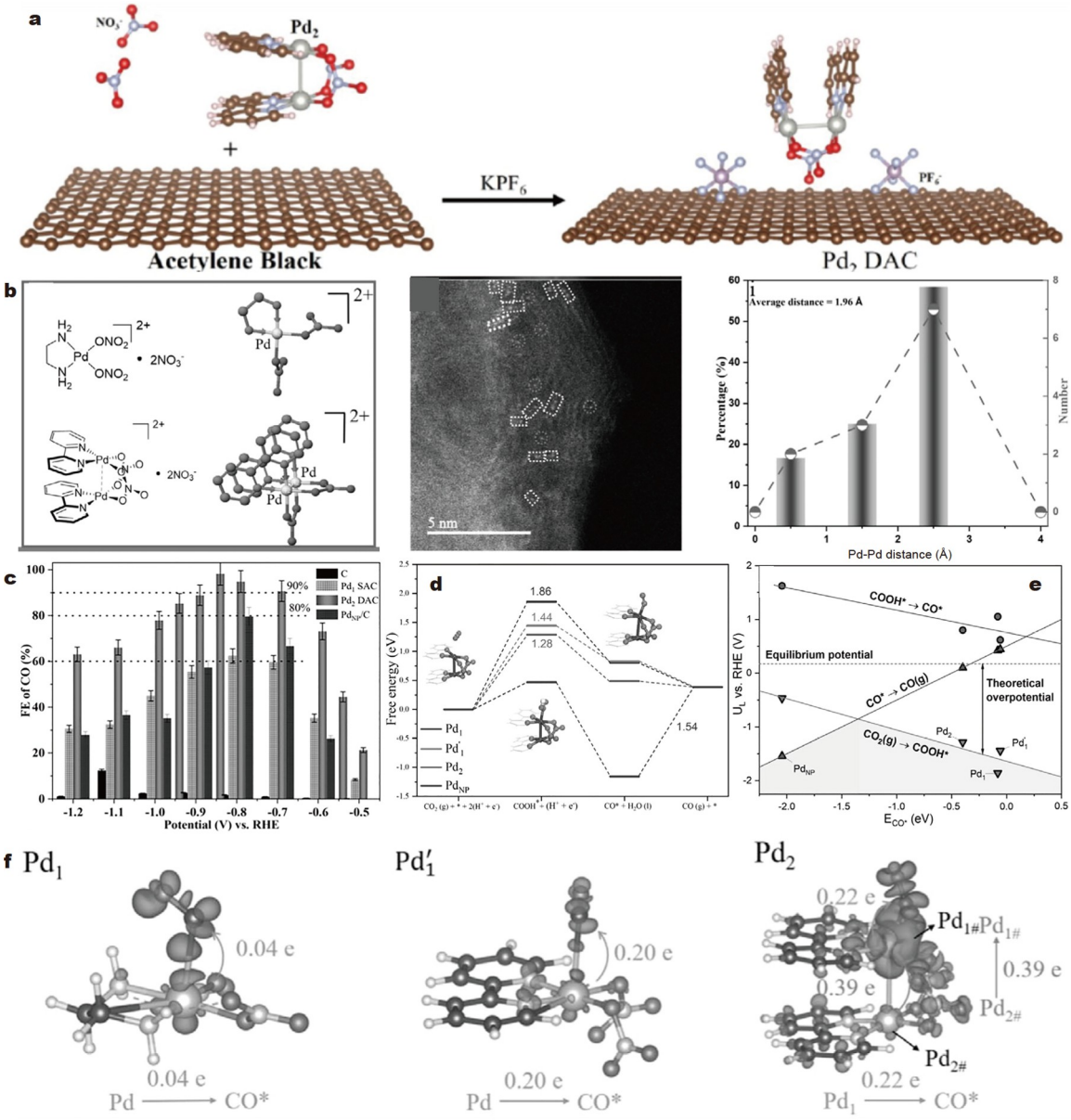

Figure 13 (a) Schematic of the preparation process of Pd_2 DASCs. (b) AC HAADF-STEM image and the corresponding Pd-Pd distance of Pd_2 DASCs. (c) FE_{CO} comparison of C, Pd nanoparticle/C, Pd_1 SAC, and Pd_2 DASCs. (d) Free energy profiles of CO_2RR on different types of Pd-based models. (e) Exploring three elementary reactions with U_L as a function of CO* adsorption energy (ΔE_{CO*}). (f) The differences in charge density of Pd_1 SAC and Pd_2 DASCs models for CO* adsorption states and the corresponding charge transfer. Reproduced with permission from Ref. [98], Copyright 2021, Wiley.

displayed that as the calcination temperature increased from 900, 1000, to 1100°C, the microstructure of Ni/NC catalysts witnessed a gradually decreased content of coordinated nitrogen for the anchored nickel atoms, accompanying a configuration evolution from single nucleation site (Ni-N_3-C), dinuclear bridging structure (Ni_2-N_4-C_2), to nickel metal cluster (Ni_4-N-C), respectively (Fig. 14d). Particularly, the Ni_2-N_4-C_2 configuration featured Ni–Ni bonding bridged two adjacent Ni-N_2-C. Ni_2 DASCs-1000 achieved above 87.0% of FE_{CO} at the overall test potentials from −0.6 to −1.0 V, and the maximum value of FE_{CO} was 96.6% at −0.8 V in 0.5 mol L^{-1} $KHCO_3$ solution (Fig. 14e). The unique metal-metal bridging structure and the proper N coordination number in Ni_2-N_4-C_2 were suggested to be responsible for the superior activity. Further DFT calculation verified that the Ni–Ni bridging structure played a positive role in modulating the electronic structure of d-states in Ni_2-N_4-C_2, thus leading to more favorable adsorption for CO_2 molecules and more profitable desorption for *CO intermediates.

Ag_2 DASCs

A dual-atom Ag_2/graphene catalyst (Ag_2-G DASCs) was prepared with binuclear Ag complex {[Ag(NO_3-O)(phtz-*N*)]$_2$(μ-phtz-*N*,*N*′)$_2$} as the precursor (Fig. 15a) [100]. For comparison purposes, single-atom Ag_1-G and Ag nanoparticles-G catalysts were achieved with mononuclear Ag complex ([Ag(phen)$_2$]NO_3) and $AgNO_3$ as the precursors, respectively. The π-π interaction between the graphene surface and the large planar aromatic structures in binuclear Ag complex enable the strong adsorption

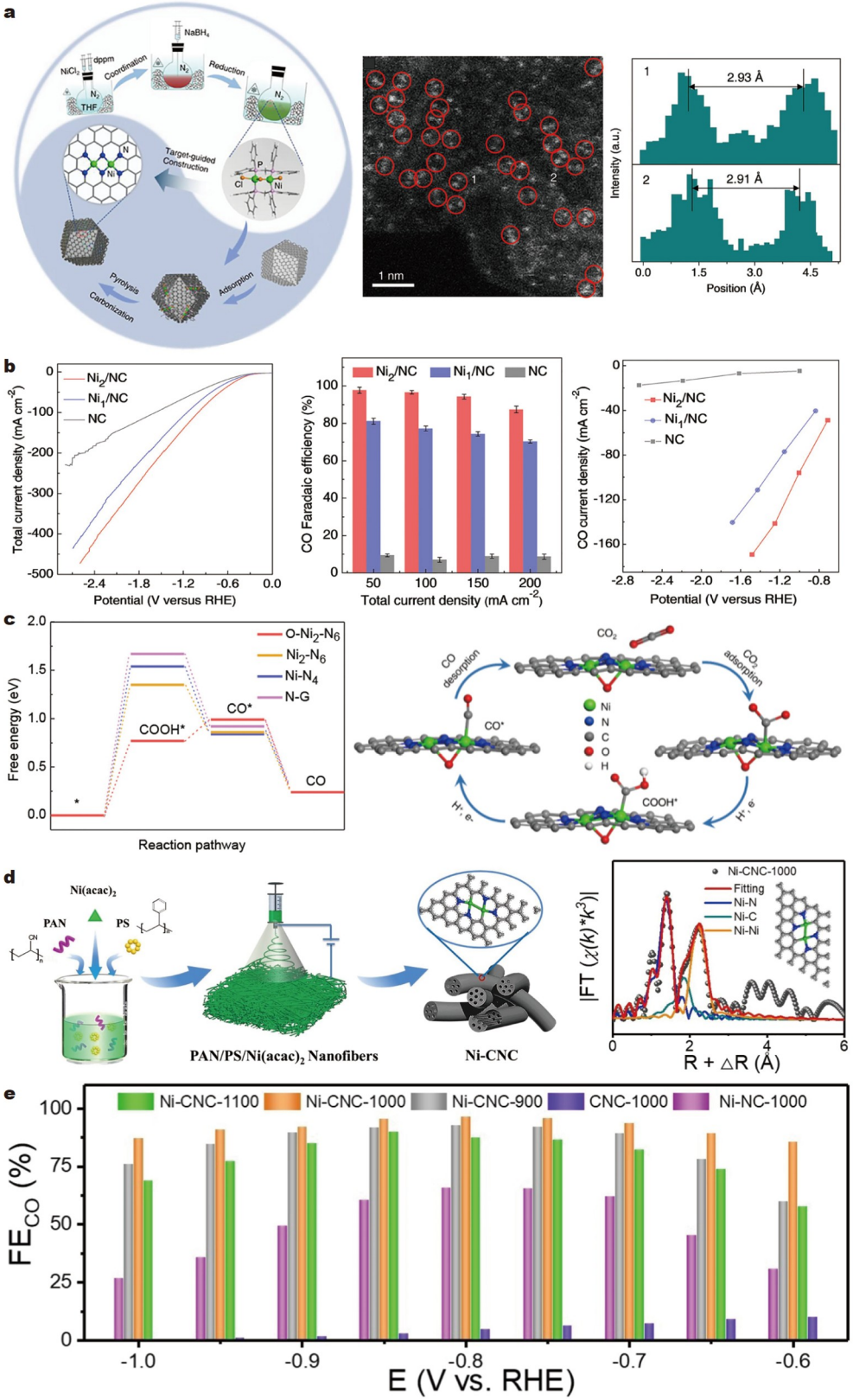

Figure 14 (a) Schematic illustration of the synthesis process of $Ni_2(dppm)_2Cl_3$ and Ni_2/NC catalyst as well as the AC HAADF-STEM image of Ni_2/NC. (b) LSV curves (left), FE_{CO} (middle), and CO current density (right) for the Ni_2/NC, Ni_1/NC, and NC catalysts. (c) Calculated Gibbs free energy diagrams and proposed reaction pathways on Ni_2-N_6 catalyst. Reproduced with permission from Ref. [64], Copyright 2021, American Chemical Society. (d) Preparation illustration and the EXAFS R space-fitting curves of Ni-CNC (Ni_2-N_4-C_2) fibers. (e) FE_{CO} of the samples with varied calcination temperatures at different applied potentials. Reproduced with permission from Ref. [99], Copyright 2022, Wiley.

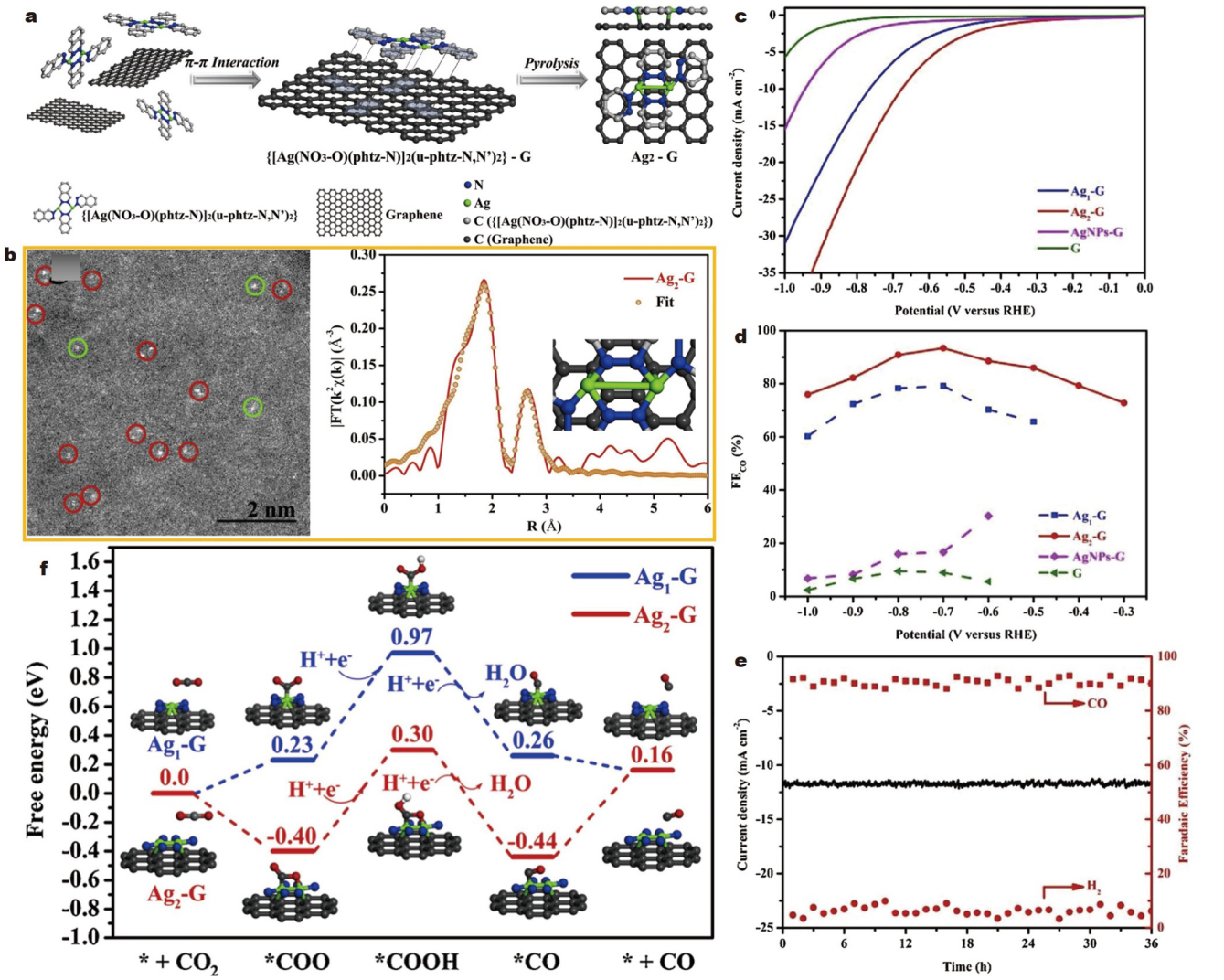

Figure 15 (a) Schematic illustration of the synthesis process of Ag_2-G catalyst. (b) AC HAADF-STEM image and EXAFS R-space fitting curve of Ag_2-G. Catalytic performance tests of (c) LSV curves, (d) FE_{CO}, and (e) catalytic stability test. Reproduced with permission from Ref. [100], Copyright 2020, Elsevier.

of precursor on the substrate. The large ligands can also provide spatial isolation for Ag_2 to prevent aggregation and separation. XANES and EXAFS results indicated the existence of Ag–Ag bond and Ag–N bond in Ag_2-G DASCs in a coordination configuration of AgN_3-AgN_3 (Fig. 15b). DFT calculations displayed that the Ag atom was anchored through *ortho*-C and *para*-C of graphene. The CO_2RR activity test of Ag_2-G DASCs showed a low potential −0.25 V *vs.* RHE to drive CO_2 reduction in CO_2-saturated 0.5 mol L^{-1} $KHCO_3$ electrolyte. The FE_{CO} reached up to 93.4% at −0.7 V *vs.* RHE, which was higher than 79% FE_{CO} of Ag_1-G and <20% FE_{CO} of Ag nanoparticles-G (Fig. 15c, d). The competing HER was suppressed as indicated by <7% FE_{H2} at −0.7 V. The current density of 11.8 mA cm^{-2} and FE_{CO} of 90% in Ag_2-G DASCs can be stabilized for up to 36 h, demonstrating superior long-term stability (Fig. 15e). Further DFT calculations suggested that the neighboring dual-atomic site in Ag_2-G can simultaneously activate the carbon and oxygen atoms in CO_2 molecules, thereby decreasing the formation barrier of *COOH, the key intermediate to CO product, by stabilizing the $*CO_2$ (Fig. 15f).

Generally, the spatial distance and the electronic configuration between the dual metal centers in DASCs dominate the selectivity and activity towards CO_2RR. Although the current product is dominated by C_1-CO, the three types of DASCs present different reaction mechanisms. For example, marriage-type DASCs that include two spatially separated different single-atom active sites demonstrate synergetic effects in CO_2RR. However, the spatial distances between dual metal centers are discrete, which severely impedes the proposal of accurate reaction mechanism. As for homonuclear DASCs, the adjacent two identical metal atoms can well regulate the adsorption energy and the state of intermediates in CO_2RR, thus achieving high selectivity to preferable product. By contrast, heteronuclear DASCs offer more opportunities for CO_2RR research due to the fact that two different metal atoms with varied atom sizes, electronegativities and electronic structures can be combined in a variety of forms. The position of d-band center can be effectively tuned by the neighboring heterogeneous atoms, thus optimizing the interaction between the active sites and intermediates in CO_2RR. The difference in the electronic configuration of heteronuclear DASCs indicates great advantages in breaking the linear scaling relationship.

CONCLUSIONS AND PERSPECTIVE

The electrochemical transformation of excessively emitted CO_2 to high-value-added fuels and chemicals provides a promising approach towards an sustainable carbon-cycle utilization. The development of high-performance catalysts with rapid reaction kinetics and high selectivity is highly desirable. In this review, we summarize the latest research advances on DASCs for CO_2RR. The classification, synthesis, and identification of DASCs are highlighted. Based on the difference in the configuration of dual-atomic active sites, the precise control of spatial distance and coordination configuration of adjacent dual-atomic sites requires both rational selection of precursors and appropriate synthesis strategies. Catalysts are categorized into marriage-type, heteronuclear, and homonuclear DASCs. The accurate identification of geometric structure and electronic configuration of dual-atomic sites is crucial for investigating CO_2RR activity of DASCs. The structure-activity relationship is in the spotlight by in-depth discussing the abilities of dual-atomic sites in manipulating CO_2 adsorption, intermediates identification and stabilization, product desorption, and HER inhibition.

Although some progress has been made, the development of DASCs is still in its early stages and faces numerous challenges in terms of synthesis, characterization, reactivity and interpretation of structure-activity relationships. (1) The development of DASCs still requires continuous efforts to develop new synthetic strategies for the precise preparation of uniform dual-atom sites with well-defined coordination and electronic structure. Uniform defects or cavities are the prerequisite for regulating the coordination, configuration, and spatial distance of DASCs [56,95,101–104]. The most commonly reported DASCs are composed of the bimetallic active sites and carbonaceous substrate with metal-C and metal-N coordination environment. It is highly desirable to expand the research on metal-nonmetal bimetallic active sites and non-carbonaceous substrate catalysts. (2) We have already described the advantages and disadvantages of the currently used AC HAADF-STEM, XAS, EELS and Mössbauer spectroscopy. The precise identifications of geometric structure and electronic configuration of dual-atomic active sites are still in its infancy. The cooperation of DFT calculations and EXAFS simulations should be more effective to elucidate the structures of DASCs. CO_2 and CO TPD experiments should be helpful to the analysis of the adsorption difference in CO_2 and *CO on DASCs [97,105]. Scanning tunneling microscopy (STM) as an important equipment for surface science investigation can potentially be applied to collect the data about electronic structure and molecular adsorbates on the dual-atom sites [72,106]. In addition, some new characterization and analytical tools at the atomic and molecular scale, such as high-resolution scanning electrochemical cell microscopy and electron backscatter diffraction [106], can be developed for the accurate structure clarification. (3) Very recent report indicated that the dynamic transformations of coordination environment and composition of CO_2RR catalyst have been verified by *operando* XAFS characterization [107,108]. The monitoring of real-time structural information of dual-atomic active sites under dynamic CO_2RR operating conditions should be further exploited by single or multiple *in-situ* or *operando* techniques to unveil the underlying reconstruction or deactivation of dual-atomic active sites [109–112]. Moreover, articulating the adsorption configuration of key intermediates is also

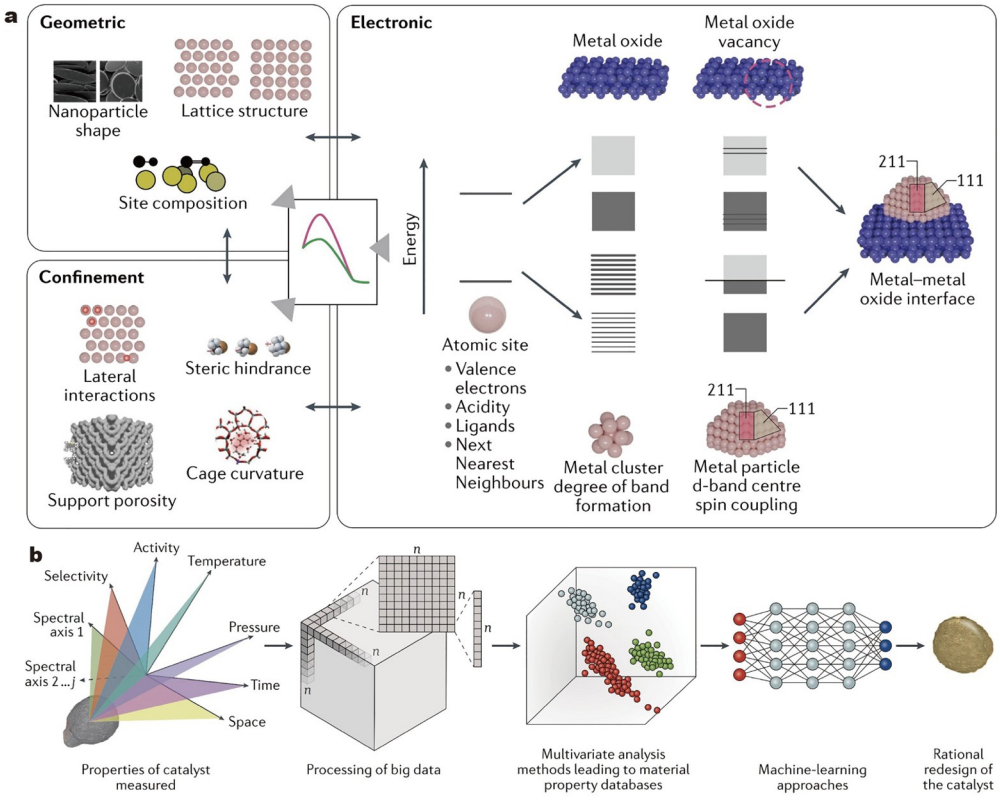

Figure 16 (a) The different parameters corresponding to geometric, electronic and confinement effects for the activity of an active site. Reproduced with permission from Ref. [116], Copyright 2022, Nature Publishing Group. (b) Parameters collected from multiple *in situ* or *operando* experiments for the rational design of catalysts. Reproduced with permission from Ref. [110], Copyright 2018, Nature Publishing Group.

very important for the analysis of reaction process. Besides the commonly used first-principles calculations approach, the molecular dynamic simulations should be more conducive to explaining the evolution process of structures [112,113]. The principles in depressing the competing HER should be well summarized. Furthermore, the relationship between how to break the linear relationship and the design concept of DASCs should be highlighted [114,115]. (4) It should be highly emphasized that although theoretical studies predict the great potentials of DASCs to obtain multi-carbon products [53,55,74], the current product is essentially CO. It is highly desired to design and develop new geometric structure and electronic configuration in DASCs, particularly referring to the types of support and dual atoms, for orderly manipulating the coupling of multi-electron and multi-proton processes towards senior products. (5) Taken all, as shown in Fig. 16, on the basis of the precise synthesis for dual-atom sites in DASC, the systematical analysis of measured properties of catalyst (geometric, electronic and confinement effects) [116] and the scientific handling of big data (activity, selectivity, conditions, spectral information, and so on) [110] present significant importance and challenges for the design of novel and efficient catalysts for high-grade products.

Received 1 June 2022; accepted 11 July 2022; published online 12 October 2022

1 Zhou Y, Zhang J, Wang L, *et al.* Self-assembled iron-containing mordenite monolith for carbon dioxide sieving. Science, 2021, 373: 315–320
2 Siegelman RL, Kim EJ, Long JR. Porous materials for carbon dioxide separations. Nat Mater, 2021, 20: 1060–1072
3 Jing H, Zhu P, Zheng X, *et al.* Theory-oriented screening and discovery of advanced energy transformation materials in electrocatalysis. Adv Powder Mater, 2021, 1: 100013
4 Wang H. Nanostructure@metal-organic frameworks (MOFs) for catalytic carbon dioxide (CO_2) conversion in photocatalysis, electrocatalysis, and thermal catalysis. Nano Res, 2022, 15: 2834–2854
5 Li J, Abbas SU, Wang H, *et al.* Recent advances in interface engineering for electrocatalytic CO_2 reduction reaction. Nano-Micro Lett, 2021, 13: 216
6 Yang D, Wang X. 2D π-conjugated metal-organic frameworks for CO_2 electroreduction. SmartMat, 2022, 3: 54–67
7 Zhou J, Liu H, Wang H. Photothermal catalysis for CO_2 conversion. Chin Chem Lett, 2022, doi: 10.1016/j.cclet.2022.04.018
8 Yang C, Gao Z, Wang D, *et al.* Bimetallic phthalocyanine heterostructure used for highly selective electrocatalytic CO_2 reduction. Sci China Mater, 2022, 65: 155–162
9 Chen FF, Chen J, Feng YN, *et al.* Controlling metallic Co^0 in ZIF-67-derived N-C/Co composite catalysts for efficient photocatalytic CO_2 reduction. Sci China Mater, 2022, 65: 413–421
10 Meng Y, Kuang S, Liu H, *et al.* Recent advances in electrochemical CO_2 reduction using copper-based catalysts. Acta Physico Chim Sin, 2020, 0: 2006034–0
11 Liu H, Zhu Y, Ma J, *et al.* Recent advances in atomic-level engineering of nanostructured catalysts for electrochemical CO_2 reduction. Adv Funct Mater, 2020, 30: 1910534
12 Gao Z, Li J, Zhang Z, *et al.* Recent advances in carbon-based materials for electrochemical CO_2 reduction reaction. Chin Chem Lett, 2022, 33: 2270–2280
13 Yang C, Zhu Y, Liu J, *et al.* Defect engineering for electrochemical nitrogen reduction reaction to ammonia. Nano Energy, 2020, 77: 105126
14 Zhang S, Sun L, Fan Q, *et al.* Challenges and prospects of lithium-CO_2 batteries. Nano Res Energy, 2022, 1: e9120001
15 Choi C, Kwon S, Cheng T, *et al.* Highly active and stable stepped Cu surface for enhanced electrochemical CO_2 reduction to C_2H_4. Nat Catal, 2020, 3: 804–812
16 Birdja YY, Pérez-Gallent E, Figueiredo MC, *et al.* Advances and challenges in understanding the electrocatalytic conversion of carbon dioxide to fuels. Nat Energy, 2019, 4: 732–745
17 Sun CY, Zhao ZW, Liu H, *et al.* Core-shell nanostructure for supra-photothermal CO_2 catalysis. Rare Met, 2022, 41: 1403–1405
18 Yang D, Zuo S, Yang H, *et al.* Tailoring layer number of 2D porphyrin-based MOFs towards photocoupled electroreduction of CO_2. Adv Mater, 2022, 34: 2107293
19 Yang D, Yu H, He T, *et al.* Visible-light-switched electron transfer over single porphyrin-metal atom center for highly selective electroreduction of carbon dioxide. Nat Commun, 2019, 10: 3844
20 Wang B, Chen S, Zhang Z, *et al.* Low-dimensional material supported single-atom catalysts for electrochemical CO_2 reduction. SmartMat, 2022, 3: 84–110
21 Zhao Q, Wang Y, Li M, *et al.* Organic frameworks confined Cu single atoms and nanoclusters for tandem electrocatalytic CO_2 reduction to methane. SmartMat, 2022, 3: 183–193
22 Cui X, Shi F. Selective conversion of CO_2 by single-site catalysts. Acta Physico Chim Sin, 2020, 0: 2006080–0
23 Monteiro MCO, Dattila F, López N, *et al.* The role of cation acidity on the competition between hydrogen evolution and CO_2 reduction on gold electrodes. J Am Chem Soc, 2022, 144: 1589–1602
24 Jiang L, Dong D, Lu YC. Design strategies for low temperature aqueous electrolytes. Nano Res Energy, 2022, 1: e9120003
25 Wakerley D, Lamaison S, Ozanam F, *et al.* Bio-inspired hydrophobicity promotes CO_2 reduction on a Cu surface. Nat Mater, 2019, 18: 1222–1227
26 Göttle AJ, Koper MTM. Proton-coupled electron transfer in the electrocatalysis of CO_2 reduction: Prediction of sequential *vs.* concerted pathways using DFT. Chem Sci, 2017, 8: 458–465
27 Nam DH, De Luna P, Rosas-Hernández A, *et al.* Molecular enhancement of heterogeneous CO_2 reduction. Nat Mater, 2020, 19: 266–276
28 Wang N, Yao K, Vomiero A, *et al.* Inhibiting carbonate formation using CO_2–CO–C_{2+} tandems. SmartMat, 2021, 2: 423–425
29 Jia Y, Li F, Fan K, *et al.* Cu-based bimetallic electrocatalysts for CO_2 reduction. Adv Powder Mater, 2021, 1: 100012
30 Ross MB, De Luna P, Li Y, *et al.* Designing materials for electrochemical carbon dioxide recycling. Nat Catal, 2019, 2: 648–658
31 Gao D, Arán-Ais RM, Jeon HS, *et al.* Rational catalyst and electrolyte design for CO_2 electroreduction towards multicarbon products. Nat Catal, 2019, 2: 198–210
32 Wang N, Miao RK, Lee G, *et al.* Suppressing the liquid product crossover in electrochemical CO_2 reduction. SmartMat, 2021, 2: 12–16
33 Gu J, Liu S, Ni W, *et al.* Modulating electric field distribution by alkali cations for CO_2 electroreduction in strongly acidic medium. Nat Catal, 2022, 5: 268–276
34 Li Y, Singh M, Zhuang Z, *et al.* Efficient reversible CO/CO_2 conversion in solid oxide cells with a phase-transformed fuel electrode. Sci China Mater, 2021, 64: 1114–1126
35 Burdyny T, Smith WA. CO_2 reduction on gas-diffusion electrodes and why catalytic performance must be assessed at commercially-relevant conditions. Energy Environ Sci, 2019, 12: 1442–1453
36 Ye K, Zhang G, Ma XY, *et al.* Resolving local reaction environment toward an optimized CO_2-to-CO conversion performance. Energy Environ Sci, 2022, 15: 749–759
37 Yang C, Li S, Zhang Z, *et al.* Organic-inorganic hybrid nanomaterials for electrocatalytic CO_2 reduction. Small, 2020, 16: 2001847
38 Meng X, Ma C, Jiang L, *et al.* Distance synergy of MoS_2-confined rhodium atoms for highly efficient hydrogen evolution. Angew Chem Int Ed, 2020, 59: 10502–10507
39 Yang H, Wu Y, Li G, *et al.* Scalable production of efficient single-atom copper decorated carbon membranes for CO_2 electroreduction to methanol. J Am Chem Soc, 2019, 141: 12717–12723
40 Liang L, Jin H, Zhou H, *et al.* Cobalt single atom site isolated Pt nanoparticles for efficient ORR and HER in acid media. Nano Energy, 2021, 88: 106221

41 Zhang H, He C, Han S, *et al.* Crystal facet-dependent electrocatalytic performance of metallic Cu in CO_2 reduction reactions. Chin Chem Lett, 2022, 33: 3641–3649
42 Yang J, Li W, Wang D, *et al.* Electronic metal-support interaction of single-atom catalysts and applications in electrocatalysis. Adv Mater, 2020, 32: 2003300
43 Zhou J, Li L, Gao XJ, *et al.* Clusterphene: A new two-dimensional structure from cluster self-assembly. Nano Res, 2022, 15: 5790–5791
44 Xue Y, Huang B, Yi Y, *et al.* Anchoring zero valence single atoms of nickel and iron on graphdiyne for hydrogen evolution. Nat Commun, 2018, 9: 1460
45 Di B, Peng Z, Wu Z, *et al.* Spatially resolved and quantitatively revealed charge transfer between single atoms and catalyst supports. J Mater Chem A, 2022, 10: 5889–5898
46 Zhong Y, Wang S, Li M, *et al.* Rational design of copper-based electrocatalysts and electrochemical systems for CO_2 reduction: From active sites engineering to mass transfer dynamics. Mater Today Phys, 2021, 18: 100354
47 Yu J, Wang A, Yu W, *et al.* Tailoring the ruthenium reactive sites on N doped molybdenum carbide nanosheets *via* the anti-Ostwald ripening as efficient electrocatalyst for hydrogen evolution reaction in alkaline media. Appl Catal B-Environ, 2020, 277: 119236
48 Lin Z, Escudero-Escribano M, Li J. Recent progress and perspectives on single-atom catalysis. J Mater Chem A, 2022, 10: 5670–5672
49 Zhang W, Chao Y, Zhang W, *et al.* Emerging dual-atomic-site catalysts for efficient energy catalysis. Adv Mater, 2021, 33: 2102576
50 Tian S, Fu Q, Chen W, *et al.* Carbon nitride supported Fe-2 cluster catalysts with superior performance for alkene epoxidation. Nat Commun, 2018, 9: 2353
51 Li K, Wang W, Zheng H, *et al.* Visualizing highly selective electrochemical CO_2 reduction on a molecularly dispersed catalyst. Mater Today Phys, 2021, 19: 100427
52 Fang B, Xing Z, Sun D, *et al.* Hollow semiconductor photocatalysts for solar energy conversion. Adv Powder Mater, 2022, 1: 100021
53 Li Y, Su H, Chan SH, *et al.* CO_2 electroreduction performance of transition metal dimers supported on graphene: A theoretical study. ACS Catal, 2015, 5: 6658–6664
54 Li R, Wang D. Superiority of dual-atom catalysts in electrocatalysis: One step further than single-atom catalysts. Adv Energy Mater, 2022, 12: 2103564
55 Zhao J, Zhao J, Li F, *et al.* Copper dimer supported on a C_2N layer as an efficient electrocatalyst for CO_2 reduction reaction: A computational study. J Phys Chem C, 2018, 122: 19712–19721
56 Chen C, Sun M, Wang K, *et al.* Dual-metal single-atomic catalyst: The challenge in synthesis, characterization, and mechanistic investigation for electrocatalysis. SmartMat, 2022, doi: 10.1002/smm2.1085
57 Zhang S, Wu Y, Zhang YX, *et al.* Dual-atom catalysts: Controllable synthesis and electrocatalytic applications. Sci China Chem, 2021, 64: 1908–1922
58 Ji S, Chen Y, Wang X, *et al.* Chemical synthesis of single atomic site catalysts. Chem Rev, 2020, 120: 11900–11955
59 Xing L, Jin Y, Weng Y, *et al.* Top-down synthetic strategies toward single atoms on the rise. Matter, 2022, 5: 788–807
60 Li Y, Xia L, Fan Y, *et al.* Recent advances in autonomous synthesis of materials. ChemPhysMater, 2022, 1: 77–85
61 Hou CC, Wang HF, Li C, *et al.* From metal-organic frameworks to single/dual-atom and cluster metal catalysts for energy applications. Energy Environ Sci, 2020, 13: 1658–1693
62 Xie W, Li H, Cui G, *et al.* NiSn atomic pair on an integrated electrode for synergistic electrocatalytic CO_2 reduction. Angew Chem Int Ed, 2021, 60: 7382–7388
63 Feng M, Wu X, Cheng H, *et al.* Well-defined Fe-Cu diatomic sites for efficient catalysis of CO_2 electroreduction. J Mater Chem A, 2021, 9: 23817–23827
64 Ding T, Liu X, Tao Z, *et al.* Atomically precise dinuclear site active toward electrocatalytic CO_2 reduction. J Am Chem Soc, 2021, 143: 11317–11324
65 Gao Z, Wang C, Li J, *et al.* Conductive metal-organic frameworks for electrocatalysis: Achievements, challenges, and opportunities. Acta Phys-Chim Sin, 2021, 37: 2010025
66 Vorobyeva E, Fako E, Chen Z, *et al.* Atom-by-atom resolution of structure-function relations over low-nuclearity metal catalysts. Angew Chem Int Ed, 2019, 58: 8724–8729
67 Ye W, Chen S, Lin Y, *et al.* Precisely tuning the number of Fe atoms in clusters on N-doped carbon toward acidic oxygen reduction reaction. Chem, 2019, 5: 2865–2878
68 Zhang N, Zhou T, Ge J, *et al.* High-density planar-like Fe_2N_6 structure catalyzes efficient oxygen reduction. Matter, 2020, 3: 509–521
69 Qu Y, Li Z, Chen W, *et al.* Direct transformation of bulk copper into copper single sites *via* emitting and trapping of atoms. Nat Catal, 2018, 1: 781–786
70 Yan H, Lin Y, Wu H, *et al.* Bottom-up precise synthesis of stable platinum dimers on graphene. Nat Commun, 2017, 8: 1070
71 Wang J, Liu W, Luo G, *et al.* Synergistic effect of well-defined dual sites boosting the oxygen reduction reaction. Energy Environ Sci, 2018, 11: 3375–3379
72 Wang Y, Su H, He Y, *et al.* Advanced electrocatalysts with single-metal-atom active sites. Chem Rev, 2020, 120: 12217–12314
73 Wang J, Huang Z, Liu W, *et al.* Design of N-coordinated dual-metal sites: A stable and active Pt-free catalyst for acidic oxygen reduction reaction. J Am Chem Soc, 2017, 139: 17281–17284
74 Guan A, Chen Z, Quan Y, *et al.* Boosting CO_2 electroreduction to CH_4 *via* tuning neighboring single-copper sites. ACS Energy Lett, 2020, 5: 1044–1053
75 Liang Z, Song L, Sun M, *et al.* Tunable CO/H_2 ratios of electrochemical reduction of CO_2 through the Zn-Ln dual atomic catalysts. Sci Adv, 2021, 7: eabl4915
76 Zhang M, Hu Z, Gu L, *et al.* Electrochemical conversion of CO_2 to syngas with a wide range of CO/H_2 ratio over Ni/Fe binary single-atom catalysts. Nano Res, 2020, 13: 3206–3211
77 Meng L, Zhang E, Peng H, *et al.* Bi/Zn dual single-atom catalysts for electroreduction of CO_2 to syngas. ChemCatChem, 2022, 14: e202101801
78 Wang L, Wang L, Du Y, *et al.* Progress and perspectives of bismuth oxyhalides in catalytic applications. Mater Today Phys, 2021, 16: 100294
79 Wang YH, Jiang WJ, Yao W, *et al.* Advances in electrochemical reduction of carbon dioxide to formate over bismuth-based catalysts. Rare Met, 2021, 40: 2327–2353
80 He Q, Liu D, Lee JH, *et al.* Electrochemical conversion of CO_2 to syngas with controllable CO/H_2 ratios over Co and Ni single-atom catalysts. Angew Chem Int Ed, 2020, 59: 3033–3037
81 Hu C, Wang Y, Chen J, *et al.* Main-group metal single-atomic regulators in dual-metal catalysts for enhanced electrochemical CO_2 reduction. Small, 2022, 18: 2201391
82 Zeng Z, Gan LY, Bin Yang H, *et al.* Orbital coupling of hetero-diatomic nickel-iron site for bifunctional electrocatalysis of CO_2 reduction and oxygen evolution. Nat Commun, 2021, 12: 4088
83 Ren W, Tan X, Yang W, *et al.* Isolated diatomic Ni-Fe metal-nitrogen sites for synergistic electroreduction of CO_2. Angew Chem Int Ed, 2019, 58: 6972–6976
84 Yang X, Tat T, Libanori A, *et al.* Single-atom catalysts with bimetallic centers for high-performance electrochemical CO_2 reduction. Mater Today, 2021, 45: 54–61
85 Li Y, Shan W, Zachman MJ, *et al.* Atomically dispersed dual-metal site catalysts for enhanced CO_2 reduction: Mechanistic Insight into active site structures. Angew Chem Int Ed, 2022, 61:
86 Pei J, Wang T, Sui R, *et al.* N-bridged Co–N–Ni: New bimetallic sites for promoting electrochemical CO_2 reduction. Energy Environ Sci, 2021, 14: 3019–3028
87 Huang Q, Liu H, An W, *et al.* Synergy of a metallic NiCo dimer anchored on a C_2 N-graphene matrix promotes the electrochemical CO_2 reduction reaction. ACS Sustain Chem Eng, 2019, 7: 19113–19121
88 Yun R, Zhan F, Wang X, *et al.* Design of binary Cu-Fe sites coordinated with nitrogen dispersed in the porous carbon for synergistic CO_2 electroreduction. Small, 2021, 17: 2006951
89 Wang F, Xie H, Liu T, *et al.* Highly dispersed CuFe-nitrogen active

sites electrode for synergistic electrochemical CO_2 reduction at low overpotential. Appl Energy, 2020, 269: 115029
90 Cheng H, Wu X, Feng M, *et al.* Atomically dispersed Ni/Cu dual sites for boosting the CO_2 reduction reaction. ACS Catal, 2021, 11: 12673–12681
91 Hao J, Zhuang Z, Hao J, *et al.* Interatomic electronegativity offset dictates selectivity when catalyzing the CO_2 reduction reaction. Adv Energy Mater, 2022, 12: 2200579
92 Zhu J, Xiao M, Ren D, *et al.* Quasi-covalently coupled Ni-Cu atomic pair for synergistic electroreduction of CO_2. J Am Chem Soc, 2022, 144: 9661–9671
93 Zhu W, Zhang L, Liu S, *et al.* Enhanced CO_2 electroreduction on neighboring Zn/Co monomers by electronic effect. Angew Chem Int Ed, 2020, 59: 12664–12668
94 Lin L, Li H, Yan C, *et al.* Synergistic catalysis over iron-nitrogen sites anchored with cobalt phthalocyanine for efficient CO_2 electroreduction. Adv Mater, 2019, 31: 1903470
95 Jiao J, Lin R, Liu S, *et al.* Copper atom-pair catalyst anchored on alloy nanowires for selective and efficient electrochemical reduction of CO_2. Nat Chem, 2019, 11: 222–228
96 Zheng QH, Chen C, Cao SM, *et al.* Well-dispersed porous Fe–N–C catalyst towards the high-selective and high-efficiency conversion of CO_2 to CO. Chin Chem Lett, 2022, doi: 10.1016/j.cclet.2022.02.078
97 Wang Y, Park BJ, Paidi VK, *et al.* Precisely constructing orbital coupling-modulated dual-atom Fe pair sites for synergistic CO_2 electroreduction. ACS Energy Lett, 2022, 7: 640–649
98 Zhang N, Zhang X, Kang Y, *et al.* A supported Pd_2 dual-atom site catalyst for efficient electrochemical CO_2 reduction. Angew Chem Int Ed, 2021, 60: 13388–13393
99 Cao X, Zhao L, Wulan B, *et al.* Atomic bridging structure of nickel-nitrogen-carbon for highly efficient electrocatalytic reduction of CO_2. Angew Chem Int Ed, 2022, 61: e202113918
100 Li Y, Chen C, Cao R, *et al.* Dual-atom Ag_2/graphene catalyst for efficient electroreduction of CO_2 to CO. Appl Catal B-Environ, 2020, 268: 118747
101 Chen Y, Ji S, Sun W, *et al.* Engineering the atomic interface with single platinum atoms for enhanced photocatalytic hydrogen production. Angew Chem Int Ed, 2020, 59: 1295–1301
102 Liu Y, Yang H, Fan X, *et al.* Promoting electrochemical reduction of CO_2 to ethanol by B/N-doped sp^3/sp^2 nanocarbon electrode. Chin Chem Lett, 2022, 33: 4691–4694
103 Zhang S, Qin Z, Hou Z, *et al.* Large-scale preparation of black phosphorus by molten salt method for energy storage. ChemPhysMater, 2022, 1: 1–5
104 Zhao Y, Liu X, Chen D, *et al.* Atomic-level-designed copper atoms on hierarchically porous gold architectures for high-efficiency electrochemical CO_2 reduction. Sci China Mater, 2021, 64: 1900–1909
105 Yang CH, Nosheen F, Zhang ZC. Recent progress in structural modulation of metal nanomaterials for electrocatalytic CO_2 reduction. Rare Met, 2021, 40: 1412–1430
106 Boucher MB, Zugic B, Cladaras G, *et al.* Single atom alloy surface analogs in $Pd_{0.18}Cu_{15}$ nanoparticles for selective hydrogenation reactions. Phys Chem Chem Phys, 2013, 15: 12187–12196
107 Ran N, Song E, Wang Y, *et al.* Dynamic coordination transformation of active sites in single-atom MoS_2 catalysts for boosted oxygen evolution catalysis. Energy Environ Sci, 2022, 15: 2071–2083
108 Nasiri MB, Iranshahi F. Comprehensive unified model and simulation approach for microstructure evolution. ChemPhysMater, 2022, 1: 133–147
109 Handoko AD, Wei F, Jenndy F, *et al.* Understanding heterogeneous electrocatalytic carbon dioxide reduction through *operando* techniques. Nat Catal, 2018, 1: 922–934
110 Meirer F, Weckhuysen BM. Spatial and temporal exploration of heterogeneous catalysts with synchrotron radiation. Nat Rev Mater, 2018, 3: 324–340
111 Yang J, Liu W, Xu M, *et al.* Dynamic behavior of single-atom catalysts in electrocatalysis: Identification of Cu-N_3 as an active site for the oxygen reduction reaction. J Am Chem Soc, 2021, 143: 14530–14539
112 Gu J, Hsu CS, Bai L, *et al.* Atomically dispersed Fe^{3+} sites catalyze efficient CO_2 electroreduction to CO. Science, 2019, 364: 1091–1094
113 Mariano RG, Kang M, Wahab OJ, *et al.* Microstructural origin of locally enhanced CO_2 electroreduction activity on gold. Nat Mater, 2021, 20: 1000–1006
114 Xiao YH, Zhang YX, Zhai R, *et al.* Helical copper-porphyrinic framework nanoarrays for highly efficient CO_2 electroreduction. Sci China Mater, 2022, 65: 1269–1275
115 Zhao ZJ, Liu S, Zha S, *et al.* Theory-guided design of catalytic materials using scaling relationships and reactivity descriptors. Nat Rev Mater, 2019, 4: 792–804
116 Vogt C, Weckhuysen BM. The concept of active site in heterogeneous catalysis. Nat Rev Chem, 2022, 6: 89–111

Acknowledgements This work was supported by Shandong Provincial Natural Science Foundation (ZR2019BB025), the Project of "20 items of University" of Jinan (2018GXRC031), and the National Natural Science Foundation of China (22071172).

Author contributions Wang H and Zhang Z proposed the topic and outline of the review paper. Qiu N and Li J collected the related information and wrote the manuscript.

Conflict of interest The authors declare that they have no conflict of interest.

Haiqing Wang is an assistant professor at the Institute for Advanced Interdisciplinary Research (iAIR), University of Jinan, after a postdoctoral fellowship at the Department of Chemistry, Tsinghua University. He received his PhD degree in 2015 from Nanjing Tech University. His current research focuses on nanostructure-controlled functional materials for energy and environmental applications including electro(photo)-catalytic water splitting, organics conversion, and CO_2 reduction.

Zhicheng Zhang is currently a professor at the Department of Chemistry, School of Science, Tianjin University. He received his PhD degree from the College of Chemical Engineering, China University of Petroleum (Beijing) in 2012. He then worked as a postdoc at the Department of Chemistry, Tsinghua University, Beijing, China. In 2014, he worked as a research fellow at the School of Materials Science and Engineering, Nanyang Technological University, Singapore. His research interests mainly focus on the synthesis and catalytic application of metalbased nanomaterials.

用于电催化CO_2还原的新兴双原子位点催化剂(DASCs)

裘娜[1†], 李俊俊[3†], 王海青[2*], 张志成[3*]

摘要 用于生产高附加值燃料和化学品的电化学CO_2还原反应(CO_2RR)为实现全球碳中和提供了一种有前景的方法. 近年来, 单原子催化剂(SACs)由于金属的最大原子利用率和独特的催化性能受到越来越多的关注. 相比之下, 除了具有单原子催化剂的上述优点外, 双原子位点催化剂(DASCs)还可以通过调节另一种相邻金属从而实现更复杂、可调的原子结构. 作为SAC的更深层次的延伸, DASCs可以为CO_2RR带来新的机遇, 最近引起了人们的浓厚兴趣. 本文中, 我们重点介绍了DASCs在提升CO_2RR性能方面的最新进展. 首先, 根据双原子活性位点的几何结构和电子配置, 对DASCs的分类、合成和证实进行了讨论. 之后, 根据结合型、异核和同核双原子位点对DASCs在CO_2RR中的催化应用进行了分类. 特别是通过系统地分析反应途径和原子结构, 详细总结了DASCs在CO_2RR中的构效关系. 最后, 提出了未来设计DASCs面临的机遇和挑战, 以启发设计具有高结构精度和高CO_2RR活性、选择性的DASCs.

